ATOMIC FORCE MICROSCOPY STUDIES OF THERMAL, MECHANICAL AND VELOCITY DEPENDENT WEAR OF THIN POLYMER FILMS

by

REGINALD H. RICE

B.S., The Citadel, 2001

A THESIS

submitted in partial fulfillment of the requirements for the degree

MASTER OF SCIENCE

Department of Physics
College of Arts and Sciences

KANSAS STATE UNIVERSITY
Manhattan, Kansas

2012

Approved by:

Major Professor
Dr. Robert Szoszkiewicz

Copyright

Abstract

Nanoscale modifications of polymer surfaces by scratching them with sharp tips with curvature radii of tens of nanometers and at variable temperatures are expected to provide wealth of information characterizing wear response of these polymers. Such studies are important in the light of understanding the nanoscale behavior of matter for future applications in advanced polymer coatings.

This thesis describes how Atomic Force Microscopy (AFM) and hot-tip AFM (HT-AFM) methods were used to characterize thermal and mechanical properties of a 30 nm thick film of poly(styrene-block-ethylene oxide), PS-b-PEO, and modify its lamellar surface patterns. Additionally, it is revealed how contact AFM and HT-AFM methods can efficiently characterize the wear response of two popular polymer surfaces, poly(methyl methacrylate), PMMA, and polystyrene, PS.

The AFM and HT-AFM studies on PS-b-PEO copolymer were aimed at producing spatial alignment of respective PS and PEO parts. Instead, however, surface ripples were obtained. These measurements are explained using mode I crack propagation model and stick-and-slip behavior of an AFM tip. In addition, HT-AFM studies allowed extraction of several thermo-physical properties of a PS-b-PEO film at local volumes containing about 30 attograms of a polymer. These thermo-physical quantities are: PEO melting enthalpy of, 111 ± 88 J g^{-1}, PS-b-PEO local specific heat of 3.6 ± 2.7 J $g^{-1}K^{-1}$, and molecular free energy of Helmholtz of 10^{-20} J nm^{-2} for the PEO within PS-b-PEO.

Utilizing a spiral scan pattern at constant angular speed and at various temperatures at the AFM tip-polymer interfaces, the wear response of PS and PMMA polymers was characterized. Cross-sections along the obtained spiral wear patterns provided plots of polymer corrugation as a function of scanning speed. From these studies it was found that the corrugation of the modified polymer surface decays exponentially with linear velocity of the scanning tip.

Table of Contents

List of Figures

List of Abbreviations

AFM	Atomic Force Microscope
HT-AFM	Hot-Tip Atomic Force Microscope
IC	Intermittent Contact
LFM	Lateral Force Microscope
MEMS	MicroElectroMechanical Systems
MLCT	Micro Lever ConTact
NC	Non-Contact
NEMS	NanoElectroMechanical Systems
PMMA	Poly(Methyl Methacrylate)
PS-b-PEO	Poly(Styrene)-block-Poly(Ethylene Oxide), note that each part of the molecule is referred to also as either PS (Chapters 2 & 3) or PEO (Chapter 2)
SEM	Scanning Electron Microscope
STM	Scanning Tunneling Microscope

Acknowledgement

I would like to give genuine thanks and gratitude to my major advisor, Dr. Robert Szoszkiewicz. His patience and understanding of how ten years in the U.S. Army can erase plenty of physics knowledge was extremely helpful. I'd like to thank our collaborators Dr. Parvaneh Mokarian-Tabari for providing our copolymer sample, Dr. William P. King for thermal AFM probes and critical readings of paper drafts, Dr. Enrico Gnecco and Dr. Reinhold Wannemacher for discussions involving the spiral section of this thesis. My sincere thanks go to Dr. Amit Chakrabarti and Dr. Bharat Ratra for being my committee members.

Lastly, but not the least, I thank my mom, Grace Rice, my wife, Jessica Rice, for support in pursuit of my interests and all the Soldiers I have served with for keeping me alive and making me successful in the U.S. Army.

Dedication

This thesis is dedicated to my daughters, Samantha and Isabella, who teach me every day how to be a better person.

Introduction

Polymers are present in nearly everything one encounters daily. Some toothpaste contain polymers such as polyethylene, the automobiles on the road today couldn't exist without polymers and the food eaten by a large portion of society is packaged, cooked and served on objects made from polymers. The amount of polymers encountered daily explodes when considering a technology dependent world. As technology starts to allow substantial miniaturization, nanoscale polymer properties and resistance to wear become of increasing importance. In particular thermal, mechanical and velocity dependant wear of polymers are the focus of this thesis.

An exciting group of polymers that may become essential to technology are copolymers. Capable of forming nanopatterns in a range of geometries, copolymers are extremely important to electronics and photonics as masks for industrial scale fabrication[1-3] and might also be used as templates for biological tissue scaffolding.[4] To unlock this potential, the geometries formed must be ordered in a manner specific to the application. Geometry of particular interest is the lamellar, or fingerprint pattern. This pattern is formed from copolymers having equal or nearly equal volume fractions of amorphous and crystalline parts[1, 5]. Through various methods, [1, 6-13] fingerprints can be ordered over a few micrometers[14-16]. This is an important step in advancement of that field, however, the methods used to achieve this alignment are very tedious. Acceleration of advancement is limited without simple methods for macroscopically ordering fingerprints and fast characterization techniques of copolymers.

With advancement of producing order geometries from copolymers, developments in microelectromechanical systems (MEMS) and nanoelectromechanical (NEMS) systems may follow. As MEMS and NEMS technologies become prevalent, the wear of individual components becomes crucial to long term operation. To reduce wear and increase the life time of these systems, individual components could use ultra thin polymer coatings. Unfortunately, these coatings are also subject to wear, thus resulting in damage or failure of the system. To allow MEMS and NEMS prevalence, accurate prediction of system component maintenance will be paramount.

Macroscopic alignment of fingerprints, characterization techniques of copolymers, and investigating wear of polymer thin films requires an instrument capable of seeing, measuring and manipulation at nanometer scales with high resolution and accuracy. Atomic Force Microscopy

(AFM) is such a powerful instrument. One AFM method, Hot-tip (HT) AFM, has already been shown to produce ordered structures known as surface nano-ripples.[17-19] HT-AFM and other methods have also probed characteristic of materials at nanometer scales.[20-23] A less exploited AFM capability is to modify morphology locally and track variations of the surface before, after, and during the modification process[18-19]. This ability is ideal for investigations of wear at nanometer scales.

This thesis uses AFM to explore thermal, mechanical and velocity dependant wear of thin polymer films. Chapter 1-Experimental Methods, introduces the reader to AFM methods, AFM hardware, AFM Software, and ends with polymer sample preparation methods Chapter 2-Local Thermomechanical Analysis of a Microphase-Separated Thin Lamellar PS-b-PEO Film, introduces copolymers, explains AFM experiments conducted attempting to induce alignment of fingerprint patterns, produces a model for nano-ripple development on the sample, and discusses how thermo-mechanical properties are derived from experiments. Chapter 3-Velocity Dependence of Nano-Abrasive Wear Obtained Using a Spiral Scan Pattern, utilized the geometric properties of an Archimedean Spiral AFM scan pattern to characterize the velocity dependence of the wear rate on polymer surfaces. This thesis ends with general conclusions of the experiments in Chapter 4. Chapter 4 also includes a section on future work in the areas covered within Chapters 2 and 3. The appendices included provide specifics on software coding, certain calculations used, calibrations of HT-AFM hardware and polymer sample preparation.

Chapter 1- Experimental Methods

1.1. Atomic Force Microscopy (AFM) methods

The first AFM was invented by G. Binning, C.F. Quate, and C. Gerber in 1986.[24] The need arose from the fact that the AFM's predecessor, the scanning tunneling microscope (STM), was limited by working only for conducting samples. Binning et al. desired a microscope that could image insulating samples. They replaced the wire of a tunneling probe of the STM with a thin strip of gold with a tiny diamond glued to the end. The movement of the gold strip was monitored by tracking the tunneling current between a wire suspended above the strip.[25] With the invention of the AFM extremely high-resolution images of virtually any sample could be obtained. Inexpensive and simple AFM systems became commercially available in 1988.[25]

AFM is primarily used to attain the topography of a sample's surface at nanometer and micrometer length scales. Nowadays, however, varieties of other AFM usages have been found. For example protein unfolding mesurements,[20] roughness of high-performance materials[21-23], nanoparticle properties[26-28], and the 14 September 2012 cover of *Science* magazine featured an AFM image of a hexabenzocoronene molecule in which bond orders and lengths of the individual bonds are distinguishable.[29] In this thesis, surface imaging, force-distance methods, and hot tip AFM methods are described and used. For a comprehensive treatise of other possible AFM modes, the reader is referred to Refs,[22, 24-26, 28-40] chapters three and four of Ref.,[25] and chapter 15 of Ref.[41] In the case of measuring the sample topography with AFM, the so-produced image is called a topograph. Figure 1.1 is a schematic of a typical AFM system. To produce topographs the AFM must 'feel' the surface with a sharp tip and build a contrast map of surface height. This map is constructed using the AFM's most critical components: the photodiode, piezoelectric scanner, and the cantilever.

The four-section photodiode measures the position of the reflected laser beam as a change in voltage between its quadrants. As the cantilever interacts with the sample surface, the position of the reflected beam changes and corresponds to a change of force at the tip sample interface. Due to the distance the laser beam travels from the sample to the photodiode, the system is very sensitive to tiny movements of the cantilever.

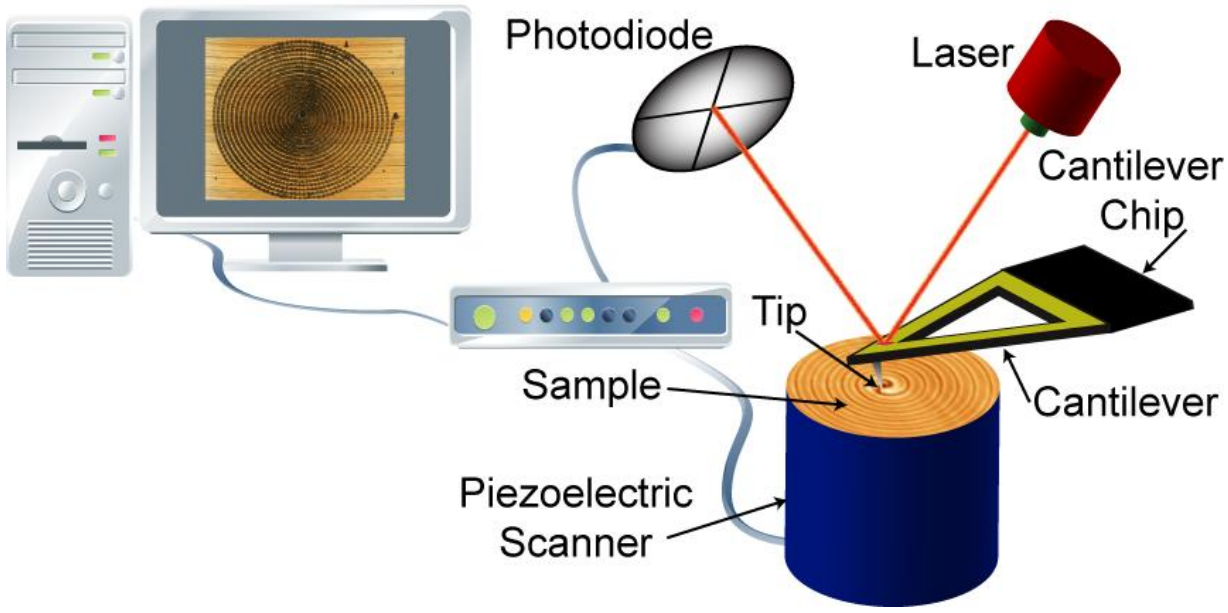

Figure 1.1. Typical AFM System. A laser beam is focused and reflects off the backside of a cantilever onto the photodetector. The photodiode, piezoelectric scanner, and the cantilever, work together to send information to the AFM hardware and software produces the topographs from the signals.

To maintain a constant tip-sample force, i.e. keep the laser dot from moving on photodiode, as the cantilever responses to topographical changes the piezoelectric scanner must also react. Scanners are piezoelectric crystals used for precise positioning of the sample with respect to the AFM cantilever, or vice versa. Their operating principle is a piezoelectric effect, i.e., size change as a function of applied voltage. Scanners of different shapes and sizes may be purchased based on the application. The most common is the tube scanner. More than 75%[25] of commercially available AFM systems use a tube scanner. The tube scanner can generate problems with topographs that will be discussed later.

No topograph would be possible without the cantilever. A large range of AFM cantilevers is available depending on applications. Most cantilevers are made of silicon or silicon nitride. Stiff levers are used to apply up to several nN of force, whereas, compliant levers are used to apply up to tens of pN of force. Cantilevers are usually either rectangular or "V"-shaped. Figure 1.2A shows both rectangular and "V"-shaped cantilevers on a model MLCT chip from Bruker. Figure 1.2B is an example of a specialized cantilever used throughout this thesis to deliver heat to the sample. The sharp tip on the end of one side of a cantilever serves as a probe. Most of the probes look like either square base pyramids or cones, although some more complicated shapes can be manufactured. This is typically done via electron beam lithography or ion beam

lithography. Typical radii of curvature at the extremity of the tips are ~10 nm and typical lengths of a tip are ~20 µm.

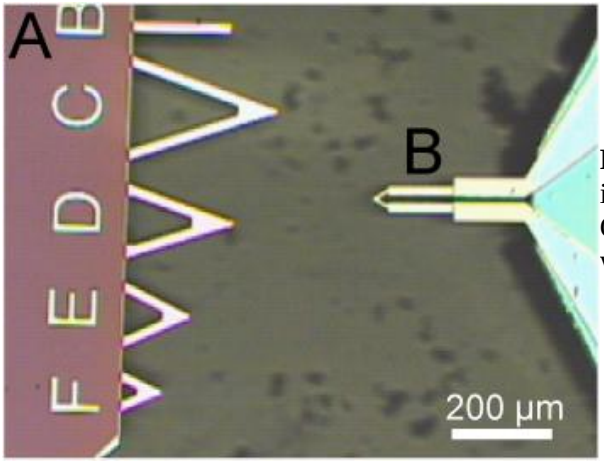

Figure 1.2. Examples of cantilevers. View is of the tip side. A) Standard MLCT Multi-Cantilever chip from Bruker in comparison with B) a thermal cantilever.

1.1.1. Surface imaging modes

There are various AFM imaging modes. The most common mode types are: contact mode non-contact mode, and tapping mode. Each mode gives different information about the sample being imaged and is useful for different situations and different sample types. Contact mode is used in this work exclusively therefore non-contact and tapping mode is discussed briefly.

Contact mode derives its name from the fact cantilever tip remains in contact with the sample at all times during scanning. In many commercial AFM systems the sample resides on top of a piezo scanner and a laser beam is reflected off of the cantilever's top side and goes to the PSPD, as in Figure 1.1. In this arrangement, the deflection signal is a measure of force and scanner movement in *Z* direction is controlled by feedback electronics. Two variations of contact mode are constant force mode and constant height mode. In constant force mode a feedback mechanism keeps the tip-sample force constant. In this mode the *Z* movement of the scanner is transformed into a topograph. Contrary is constant height mode. Here the feedback is turned "off"; so the *Z*-height of the scanner remains constant resulting in changes in the deflection signal from a cantilever creates the topograph.

In non-contact (NC) mode, the cantilever tip is held between 5 to 100 nm above the sample surface. The cantilever is vibrated with amplitude of tens of nanometers with a constant frequency near the resonant frequency for the cantilever. The amplitude and frequency of the cantilever's vibration change in response to force gradients which vary with the tip-to-sample distance as the tip scans over the sample surface. The change in vibration amplitude or frequency, respectively, is followed upon and transformed into a topograph by AFM computer

software. Since the tip does not touch the surface NC mode is ideal for soft polymers and biological samples. Intermittent-contact (IC) or tapping mode is similar to NC mode, but in IC mode, the vibrating cantilever briefly contacts the sample within its each oscillation period.

1.1.2. Force-distance (FD) curves

Besides imaging, the AFM is often used to record FD curves. This is done by monitoring the deflection, i.e., force, of the cantilever during approach, contact and withdrawal, i.e., change of distance, from the sample surface. The FD Curves are recorded without scanning in the X or Y direction. The operator of the AFM controls multiple aspects of the FD curve such as maximum deflection, e.g., maximum contact force, speed of the sample to the tip and many others. The resulting FD curve is a measure of cantilever deflection verses vertical distance traveled by the sample. The forces exerted on the tip by the sample are often used in calibration of the spring constant of the cantilever.

1.1.3. Hot-tip (HT) AFM

Hot-tip AFM (HT-AFM) is an ensemble of AFM methods to produce local topographical and/or chemical change to the surface using heat transferred from the tip of a thermal cantilever. These cantilevers were originally developed for data storage applications.[42] From there they have been used to locally chemically modify certain polymers[18, 43-44], create conducting nanoribbons on graphene[45] and have found to be very useful in metrology[46], thermophysical property measurements,[47-49] and manufacturing at the nanoscale.[19] Figure 1.2B gives an example one of the thermal cantilevers used in chapters three and four. The heating of the tip is achieved by the different levels of silicon doping. With the Si above the tip doped less than the legs the tip becomes more resistive then the legs and will heat up with applied voltage. Figure 1.3 shows the set-up used to send voltage across the tip. Heating power is applied by an external generator and a resulting voltage is measured across an external resistor in series with the HT-AFM cantilever. Such an arrangement protects the lever from sudden voltage spikes, and allows a reproducible way of electrical power delivery to the tip.

The uniqueness of the HT-AFM is irrelevant if one cannot accurately know the temperature of the tip, and consequently on temperature at the tip-sample interface. To calibrate the temperature on the polymer surface two calibration steps are needed. First, one needs to find out the temperature on the tip as a function of the power delivered. Second, the calibration factor

relating the temperature on the tip to the temperature on the tip-sample interface needs to be obtained. Temperature of the cantilever tip cannot easily be measured directly, but it has been found to be linearly related to the power delivered to the cantilever.[46] Thus, to find the tip temperature means to relate the temperature of the tip to the applied generator voltage measured across a known resistor with a voltage meter. The resistance of the cantilever varies with temperature, but one needs some reference points, i.e., to say that at such and such resistance the temperature is such and such. Room temperature and initial cantilever's resistance to a very small voltage provides a first reference point. Another one is obtained as follows. Due to the differing levels of doping,[50] once the tip reaches a certain temperature the resistance of the tip drops sharply. This is called the thermal runaway and occurs at 550° C for the HT-AFM cantilevers used in this work.[46] Once the tip temperature is known, the tip-sample interface temperature is found here by following the work of Hinz et al.[30] FD curves are performed at various temperatures on silicon; this provides a reference for cantilever deflection. Then, FD curves are performed on polymer samples with well known softening temperatures and at various tip temperatures. Once the indentation slope of the FD curves decreases and the loading and unloading parts of the FD curves start to separate substantially the tip-sample interface has reached the softening temperature of a given polymer sample. See Appendix A for more details.

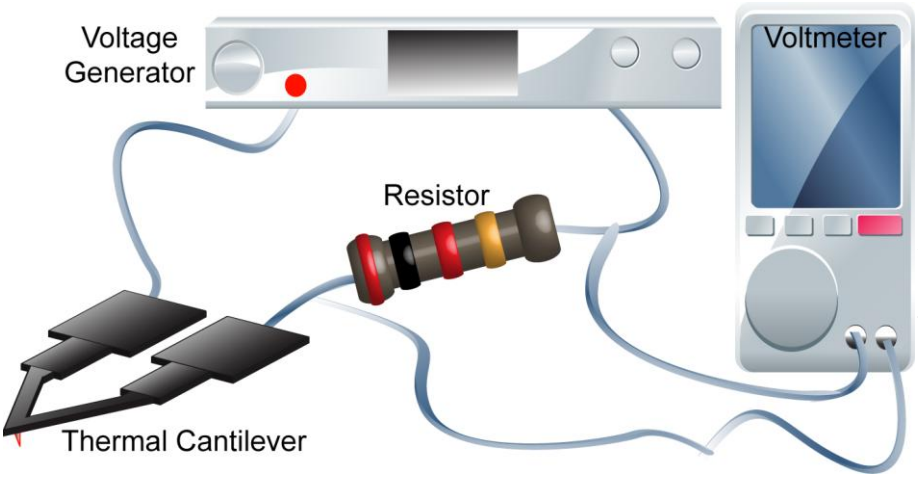

Figure 1.3. HT-AFM Set up. The components used to deliver voltage to the thermal cantilever and measure the resulting voltage.

1.1.4. Spring constant calibration of cantilevers using a thermal method

To obtain an accurate force applied to the sample the spring constant of the cantilever must be known. Manufacturers of cantilevers provide a nominal spring constant, but an actual value for each cantilever can be significantly different. In this thesis the thermal method

originally developed by Hutter and Bechhoefer is used. [33, 36] Using a custom-made AFM system in our lab[20] the elastic spring constant, k, for cantilevers was calibrated as follows :

$$k = \frac{k_B T}{< x^2 >} = \frac{k_B T}{Power * Slope^2}$$

where: k_B is the Boltzmann's constant, T is temperature in absolute scale, and $<x^2> = (Power)*(Slope)^2$ is the mean square deflection of the cantilever, where "*Power*" is the area under the fundamental resonant frequency, shown in Figure 1.4 and "*slope*" is the ratio of extension (in nm) to force (in volts) when the cantilever is in contact with the surface. The corrections and other important aspects of thermal calibration are described extensively in Ref. [20, 33, 36]

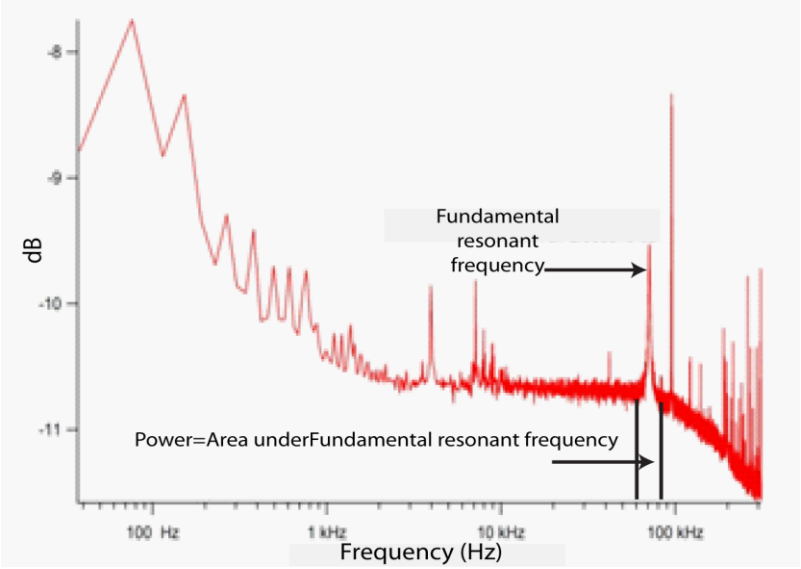

Figure 1.4. Example of power for calculations of cantilever spring constant. Shown is the fundamental resonant frequency for a thermal cantilever.

1.1.5. AFM limitations and imaging artifacts

The AFM is a very versatile system but it has limitations like any other experimental set-up. The AFM system "feels" the sample surface and from this process, imaging artifacts can arise. Artifacts can be due to the following: tip profile, X-Y-Z couplings of various sorts, sensing of additional kinds of surface forces, various kinds of noise, AFM feedback and poor cantilever selection.

The common cause of artifacts topographs is the shape of the tip. Usually the tip is a cone with spherical or paraboloidal ending characterized by a radius of curvature between 10nm and 100nm. This is important when dealing with nm size surface features. The measured lateral size of such features will seem larger by geometrical arguments because of convolution with the tip profile. Furthermore, wear of the tip from repeated use will also change the tip profile. The tip

can pick up debris from the samples surface. Additionally, manufacturing mistakes lead to tip profile artifacts such as; double, tilted, and non-centered tips. To characterize accurately the given shape of the tip, the tips can be scanned over a calibration grating or imaged with a scanning electron microscope.

Additional kinds of surface forces can also create scanning artifacts. A local change in elasticity and adhesion of the sample at the tip-sample contact produces change in attraction or repulsion between tip and sample. This causes the laser position to suddenly change on the photodiode and will produce a deviation in the topograph.

Unwanted X-Y-Z couplings in cantilever and scanner displacements are as follows. Only one end of the cantilever is clamped to the cantilever chip, which is visualized by the black box in Figure 1.5A. This causes tip movements to be parabolic, not linear, so any displacement in one axis is coupled to the other two axes. The scanners couplings originate due to the AFM scanner being a tube. Figure 1.5B illustrates how a displacement in one direction induces additional displacement in other directions. Some accountability on the X-Y-Z couplings in the scanner displacements comes from internal calibrations of the scanner, which has its own X-Y-Z position sensors. In the AFM set up used in this work, the sample resides on top of the scanner and the tip is brought into the contact with the sample by motors in the AFM head, where the tip resides. Thus, the X-Y-Z couplings in the scanner and in the cantilever add up. These effects are often small enough not to interfere with typical scanning conditions used in this work.

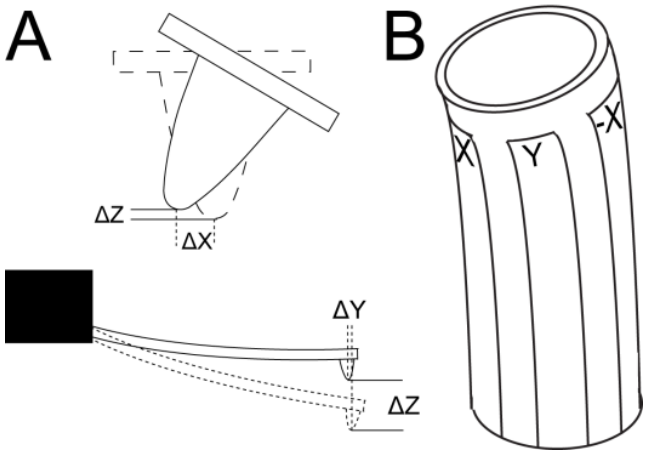

Figure 1.5. X-Y-Z coupling. This exaggerated carton of scanner movement shows how movements of the cantilever and/or scanner can result in displacements in other directions.

Three types of noise are detrimental to AFM measurements: mechanical, thermal and electronic. Mechanical noise reduction is accomplished through the AFM system placed on a float table with minimal cables connecting the AFM to the computers. Also, warnings during scanning are placed on the lab door to alert others to move slowly while entering. Thermal noise

is reduced simply by allowing the equipment to warm up for 30 minutes. The scanner becomes heated as several hundred volts are applied; the 30 minute warm up allows the scanner and surrounding components to become approximately the same temperature. The electronics can add additional noise that is electromagnetic in nature. This noise can interfere with the feedback electronics and produce topographs with unreliable data. Reduction of this is achieved by proper wire insulation and the use of covers over the AFM system.

AFM feedback and poor cantilever selection is more connected to the AFM operator then to the microscope itself. Nevertheless, these two pitfalls will generate substantial artificial topographical information if improperly executed. If AFM feedback is set too low, surface tracking quality suffers and the tip may miss surface features. On the contrary, when too high, a tiny topography change will cause the system to over react and produce topography spikes. This overreaction of the system may also cause the scanner to move fast enough to excite cantilever's vibrations at its resonances, and thus additional artificial topography. Cantilever selection is therefore crucial also. A very stiff cantilever may destroy a soft sample during imagining, if too compliant the movement of the cantilever will be large even over small topographical changes. If improper AFM feedback settings are combined with poor cantilever selection topographs become extremely defective. Overall, the sample stiffness and the cantilever's stiffness should be similar and the feedback settings should be tested to minimize these artifacts.

1.2. Preparation of custom thickness polymer films by a spin coating method

Spin coating a dilute solution is a common way to produce uniform thickness polymer films on a substrate of choice. Figure 1.6 presents the equipment and supplies used for spin coating. When producing a sample an excess amount of solution is placed on a substrate and then rotated at high speeds. This causes the solution to spread evenly over the substrate, expelling excess and evaporating the solvent out of the solution. The thickness of the film depends on spinning time, liquid density, spin speed, and initial solution viscosity[51]. Many models[51-54] have been purposed to predict film thickness and work well to get the film within a range of thickness. Because of variations in the predictions of the models, the scratch test is performed to measure sample thickness. The scratch test is nothing more than using a razor blade remove the polymer film to the substrate (glass or silicon so intents into the substrate can be ignored) and measuring the thickness change via a surface profiler or an AFM. Appendix D contains a detailed preparation procedure for creating a thin polymer sample used in this work.

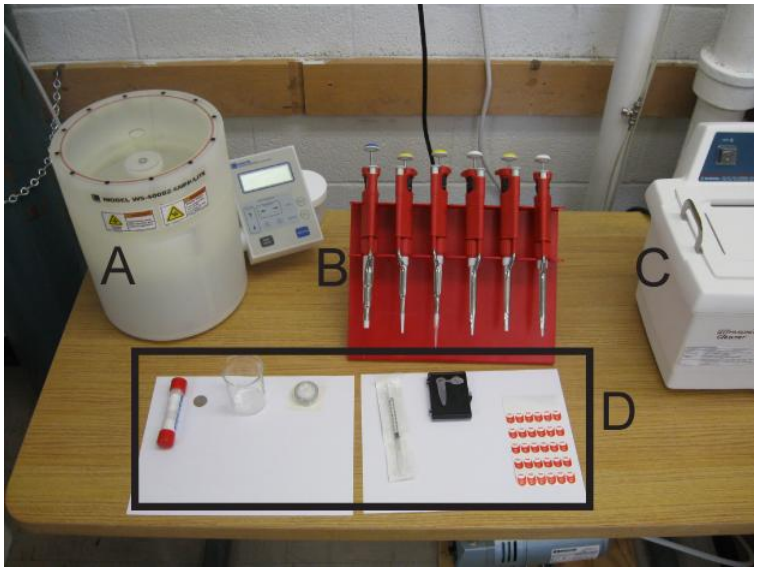

Figure 1.6. Spin coating equipment. Tools used during the spin coating process to produce samples. A) Spin coater, Model WS-400E-6NPP-LITE, Laurell Technologies Corp., B) Pipettes, C) Ultrasonic Cleaner, Model 2510 Branson Ultrasonics Corporation, D) Sample preparation materials, see Appendix D for detail on the use of these materials.

1.3. Hardware methods

The AFM topographs and thermal tip experiments were conducted using a di-CP-II AFM, di-CP-II Controller, Proscan software, both from Bruker USA, and IGOR Pro software from WaveMetrics, Inc. Figure 1.7 illustrates the hardware setup used in the case of the controlled polymer imaging. The schematic HT-AFM setup has been produced in Figure 1.3.

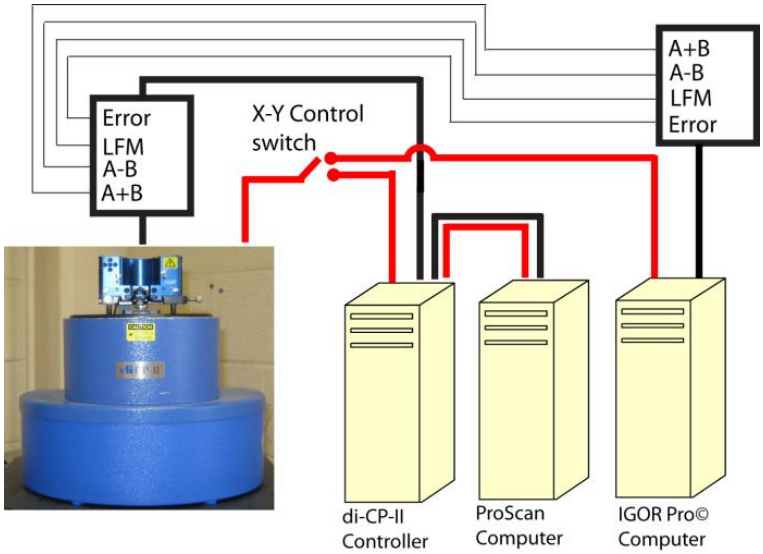

Figure 1.7. AFM hardware. Schematic of the AFM control and data recording hardware. Red lines indicate control signals to the AFM while black indicate data signal output and recording. In the figure the toggle switch is in the "external" position giving the IGOR Pro computer control of the X-Y movement of the scanner.

Signals are sent to and recorded from the AFM through the di-CP-II controller. Using a signal access module, the data signals from the AFM can also be recorded by a data acquisition card in the IGOR Pro computer.

To override the di-CP-II controller, a toggle switch was installed by the Kansas State University Electronics Lab on the back of the di-CP-II controller. The switch is labeled "XY-

Internal" and 'XY-External". Internal means the di-CP-II controller and Proscan software control all AFM functions while external gives X-Y control of the scanner to the IGOR Pro computer. There is also a custom switch for Z axis control but is not used in this thesis. The XY-External setting allows the IGOR Pro computer to send voltage signals for X-Y position control to the scanner directly, while the di-CP-II controller still maintains Z-axis position control (Z switch remains on internal).

1.4. Software methods

The AFM alone is a very elaborate paperweight. The AFM needs software to create topographs, conduct experiments, record and measure data or move the scanner. Therefore when using an AFM system one must rely on multiple computer software programs. The most prevalent programs used in this work are Proscan, WSxM, and IGOR.

Proscan version 1.9 is the factory software to control the di-CP-II AFM. It is Microsoft Windows based software that has simple to use command boxes to control all aspects of AFM operations. These controls enhance the quality of topographs, allow the operator to generate FD curves, change the scanning size/speed, move the tip on the surface, plus many others. Most important it is the user interface with the di-CP-II controller and allows commands to be given to the microscope.

Windows Scanning x Microscope (WSxM) version 5 is commercial but free software from Nanotec Electronica available at http://www.nanotec.es/products/wsxm/download.php. Like Proscan, it is designed to control an AFM system produced by Nanotec Electronica. The advantage to WSxM is the included image processing software, which seems easier to use and more powerful that the Proscan image processing software. The WSxM processing software allows the user to measure topographs along curved profile lines. It also has the ability to save topograph files with profile lines embedded on the image for later use. These features proved invaluable while processing topographs for this thesis. Other notable AFM image processing software includes Gwyddion, and many other programs exist and are listed in Appendix C of Ref.[25], but WSxM was simple to use and contained the best features to quickly transfer topograph data to IGOR Pro software.

The software workhorse is IGOR Pro. IGOR is a commercial Windows based software environment from Wavemetrics, USA. It is used both for data processing and acquisition. Igor processes large data sets quickly, can acquire the AFM data through a data acquisition card

(here: PCI-6289 from National Instruments), and is programmable. The programmability of IGOR is most important to generate custom and calibrated AFM scan patterns. This is because, the scan pattern generated by the di-CP-II controller is a raster pattern extending out and back along the fast scan axis, normally X, and moving up incrementally along the slow scan axis, normally Y. This was verified using a 64 line scan over a 60 μm^2 area, allowing visual confirmation of the scan pattern through a microscope. This pattern is ideal for general imaging, but seriously limiting achieving any other possible scanning geometry. For example, to explore sample reactions with the tip on nanometer scales one scan line cannot interfere with the previous. Appendix A contains specific Igor software coding used in the following chapters to generate custom scanning patterns. Lastly, graphics produced by IGOR are easily formatted to publication quality with minimal effort.

Chapter 2- Local Thermomechanical Analysis of a Microphase-Separated Thin Lamellar PS-b-PEO Film

The work in this chapter has been done in collaboration between Reginald H. Rice and Dr. Robert Szoszkiewicz with Dr. Parvaneh Mokarian-Tabari and Dr. William P. King. Dr. Mokarian-Tabari is with the Materials Research Group, School of Chemistry and the Tyndall National Institute, University College Cork, and Centre for Research on Adaptive Nanostructures and Nanodevices, Trinity College Dublin, Ireland. Dr. Mokarian-Tabari provided the copolymer sample and insight to experimental findings. Dr. King is with the Department of Mechanical Science and Engineering, University of Illinois Urbana–Champaign. Dr. King provided the thermal cantilevers used in this chapter, and helped to write a manuscript describing these findings. Finally, Dr. Amit Chakrabarti is acknowledged for discussion about arrangements of copolymer molecules on the silicon surfaces.

2.1. Introduction

Diblock copolymers having equal or nearly equal volume fractions of amorphous and crystalline parts often display the "fingerprint-like" lamellar morphology,[1, 5] with a mean spacing between neighboring fingerprint lines of several tens of nanometers. Directional ordering of lamellar fingerprints over mesoscopic lengths has potential applications in electronics and photonics, for example, as masks for industrial scale fabrication of microprocessors and UV diffraction gratings.[1-3] Ordered nanopatterns might also be used as templates for biological tissue scaffolding.[4] Many strategies to align the lamellar fingerprint-like structures use tediously prepared substrates obtained via a combination of topographical[6] and/or chemical substrate patterning,[7] graphoepitaxy, epitaxial crystallization, and substrate's modification with polymer brushes.[1, 8-10, 14] Other approaches manipulate annealing conditions by using electric fields,[11] shear forces,[12] solvent fields,[55] thermal gradients,[8, 13] and combinations of conditions as in a stepwise thermo/solvent annealing.[56] Using some of these methods, few micrometers long fingerprint structures have been obtained for several asymmetric block copolymers.[14-16] However, a simple method for producing macroscopically ordered fingerprint areas and fast characterization techniques are needed to advance in this field.

Application of local heat and force to copolymers via HT-AFM techniques is well suited to organize polymer nanopatterns. Rapid heat flows and sharp temperature gradients in the

vicinity of a heated AFM tip can achieve a topographical modification of the polymer surface.[18, 34, 46-47, 57-58] For example, force and heat applied while scanning amorphous polymers with thermal AFM cantilevers have produced ordered structures known as surface nano-ripples.[17-19]

In this chapter AFM and HT-AFM[17-18, 34, 58-59] methods are used to modify fingerprint alignment and thermophysically characterize an ultra-thin film of nearly symmetric PS-b-PEO. A fingerprint pattern of lamellar PS-b-PEO is obtained on "as received" silicon substrate, that is, without any underlying polymer brush or surface modifications. Next, investigations of several strategies to align the fingerprint pattern via AFM scanning at various conditions are conducted. These investigations yield either abrasive surface patterns or surface nano-ripples and not macroscopically ordered fingerprints. The evolution of lamellar patterns is explained by the polymer film molecular structure and mode I crack propagation in the polymer[60] combined with stick-and-slip effects of the AFM tip.[61] By comparing AFM scans obtained at various tip-sample temperatures and at several scanning conditions the PEO melting temperature, T_m^{PEO}, and the PS glass transition temperature T_g^{PS} is calculated. The number of PS-b-PEO molecules affected mechanically and thermally at each contact point between an AFM tip and a polymer surface is found using elastic contact mechanics and heat propagation models. Then, at the tip-polymer contact points in the vicinity of T_m^{PEO} and T_g^{PS} revealed the PS-b-PEO specific heat, the PEO melting enthalpy, and the free energy of Helmholtz for PEO folding (and melting).

2.2. Materials and Methods

The polymer was a PS-b-PEO diblock copolymer from Polymer Source, with number average molecular mass $M_{n,\mathrm{PS}}$ = 12.3 kg mol^{-1} and $M_{n,\mathrm{PEO}}$ = 14 kg mol^{-1}, polymer polydispersity 1.09, an average polymer density 1.1 g cm^{-3}, and a PEO volume fraction of 52%. The PS-b-PEO film was produced by spin coating and stepwise thermo/solvent annealing directly onto a Si substrate.[62] Spin coating was done 3000 rpm for 30 s and from 1 wt % polymer solution in HPLC-grade toluene from Sigma-Aldrich, USA. In the stepwise thermo/annealing process the films of PS-b-PEO were thermally annealed in a vacuum oven at 90 °C for 150 minutes, and then cooled to 77 °C, which is still above the PEO melting point. The samples were then removed from the oven and placed in a 100 ml vessel with HPLC-grade toluene and DI water reservoirs and returned to the oven at 66 °C and annealed for additional two hours at 40 °C, which is also above the PEO crystallization temperature.[56] The resulting film thickness of 30 ± 2 nm was determined by a scratch test with AFM.

The AFM topographs of the PS-b-PEO were recorded in contact mode with the di-CP-II AFM system, photographed in Figure 1.7, Proscan software, and SiN_x MLCT-D cantilevers, see Figure 1.2A. The cantilevers had a nominal elastic spring constant between 0.03 to 0.05 N m^{-1}. For scanning at various tip-sample temperatures the HT-AFM set up in discussed in Chapter 1.1.3. was mounted in the di-CP-II. The tip temperature calibration was based on methods covered in Appendix C and the elastic spring constants of the cantilevers found with techniques in Chapter 1.1.4.

2.3. Results

2.3.1. Micro- and nano-scale topography of the PS-b-PEO films

Figure 2.1A presents a typical 50 μm by 50 μm AFM topograph of the PS-b-PEO film. The fingerprint morphology in Figure 2.1B has a pitch of 39 ± 3 nm and displays local order on the length scales up to several hundreds of nanometers. Every 5 – 10 μm the polymer surface shows two other kinds of uniformly distributed structures: bubbles in Figure 2.1C and craters in Figure 2.1D and 2.1E. The bubbles are several microns wide and ornamented by fingerprints. Their base is 11 ± 3 nm below the surrounding surface and has RMS roughness of 0.3 nm. The craters are several micrometers long. Their base is 29 ± 2 nm below the surrounding surface and has a typical Si surface roughness, so it must be the Si substrate. Distinct dendrites with height of 12 ± 2 nm above the Si substrate grow from their perimeters towards the center.

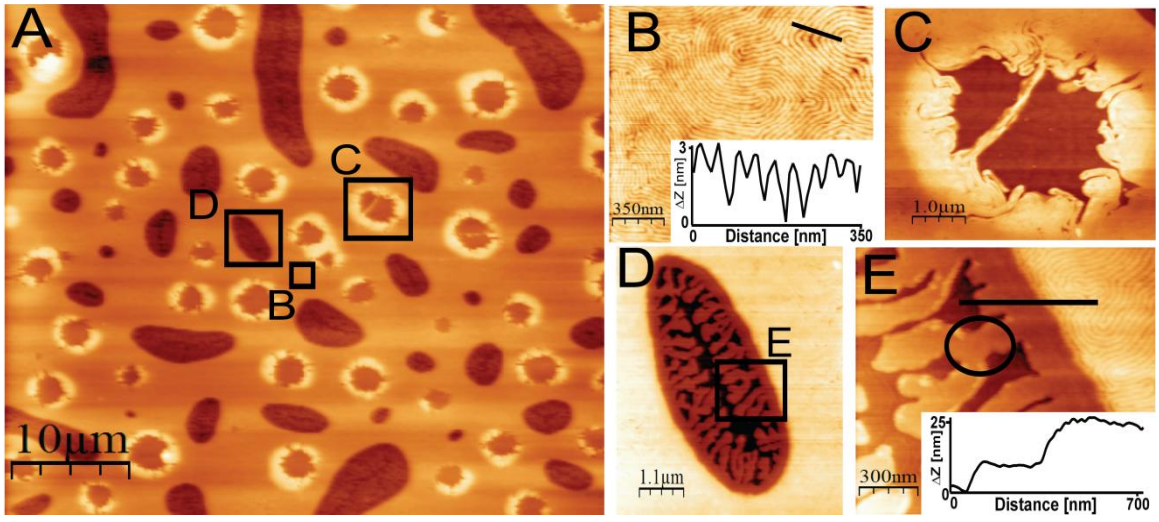

Figure 2.1. General topography of the PS-b-PEO film. A) 50 μm x 50 μm AFM topograph of the PS-b-PEO film stepwise thermo/solvent annealed on silicon substrate. B) Fingerprint pattern showing local order. C) Example of a bubble. D) An example of a crater. E) Dendritic structures within a crater with a topography cross section on the inset and a characteristic tip splitting event marked by a black circle.

2.3.2. Application of local force to align the fingerprint pattern

Figure 2.2 shows a 0.9 μm by 0.9 μm area within a 2.9 μm by 2.9 μm zone of a fingerprint pattern scanned using an MCLT-D cantilever at 1 μm/s scanning speed and 3 nN AFM tip-sample contact force (setpoint). Upon scanning fingerprints developed into ripples.[17, 19, 35, 63-65] The pattern spacing, λ, stabilized at 105 ± 10 nm in about 10 rescans. After 15 scans, the value of λ increased to 120 ± 10 nm and after 21 scans it jumped to 135 ± 10 nm. Similar experiments at higher tip-sample contact force did not produce any fingerprint alignment, but showed faster change to the ripple pattern. Thus, force alone did not produced alignment of the fingerprints, and prolonged scanning produced ripples.

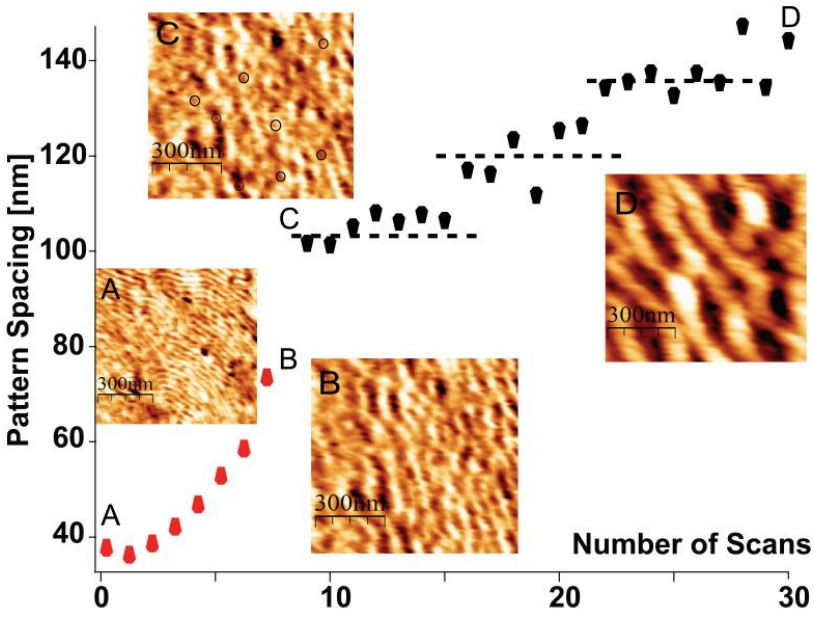

Figure 2.2. Pattern spacing plotted against the N scans. Dashed lines mark local plateaus. Inset: the AFM topographs showing evolution of fingerprints after A) *N*=1 B) *N*=8, C) *N*=9, and D) *N*=30.

2.3.3. Application of local heat to induce fingerprint alignment

Next, the fingerprint morphology was heated by cantilevers with integrated heaters (thermal levers) at the tip-polymer interface and at the lowest setpoints (1 to 3 nN) to allow consistent contact between the tip and the surface. First, a series of contact mode scans at a constant tip temperature modified the polymer surface. Figure 2.3 presents two AFM surface topography rescans obtained after one and six scans with a thermal tip at 32 ± 3 °C yielding 28 ± 7 °C at the tip-polymer interface. Topographs in Figure 2.3 were obtained with a MLCT-D cantilever at a setpoint of less than 3 nN to minimize any additional surface change. The pattern in Figure 2.3B has a period of 100 nm. Thus, these are rather ripples rather than fingerprints.

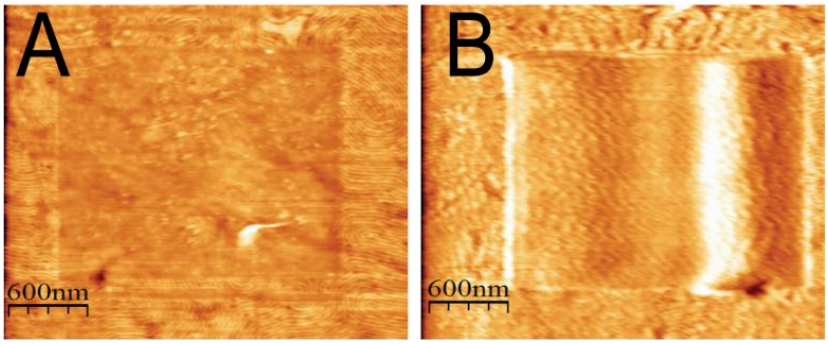

Figure 2.3. Multiple force only scans. AFM topographs of a polymer surface after *N* scans with a thermal tip at 28 ± 7 °C. A) *N*=1, B) *N*=6. Heated areas are in the middle.

Also, the effects of a single scan with a heated tip were investigated in thermally modified smaller-scale areas of 2 μm by 2 μm and larger-scale areas of 50 μm by 50 μm. Figure 2.4 and Figure 2.5 show the respective contact mode rescans with a MLCT-D lever at <3 nN setpoints. In both cases initial scans with a thermal tip contained 256 scans lines with 256 data points along each line, which is why some lateral line spacing of 200 nm shows up in Figure 2.5C-F. Despite local thermal modifications comprising only several PS-b-PEO molecules at a time, no thermally induced alignment of the fingerprints was evident. Imaging at setpoints >10 nN destroyed the film quickly, see Figure 2.6, and other scanning rates did not produce noticeable alignment of the fingerprint pattern either.

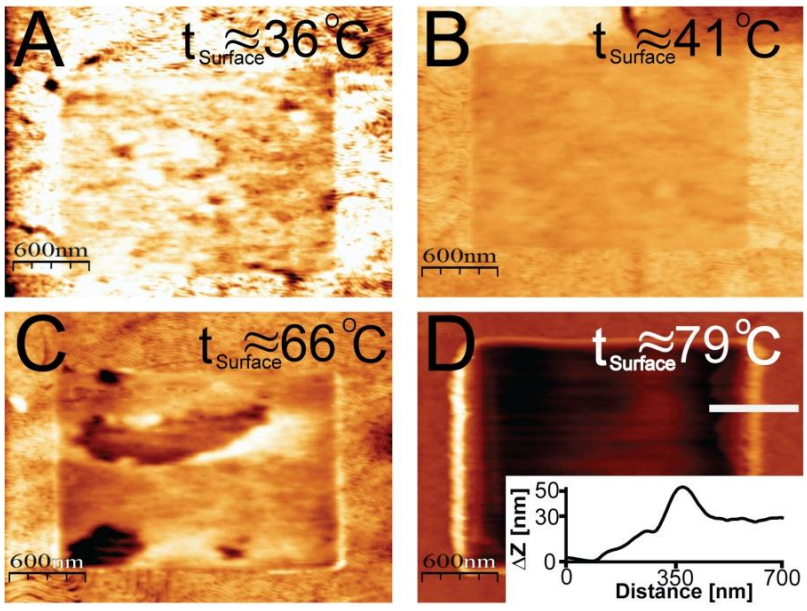

Figure 2.4. Single scans with thermal tip. 3 μm x 3 μm AFM topographs of a polymer surface after a single scan with a thermal tip in 2 μm x 2 μm areas modified at tip-polymer interface temperatures of: A) 36 ± 8 °C, B) 41 ± 8 °C, C) 66 ± 10 °C, and D) 79 ± 11 °C, the inset shows a cross-section along the white line.

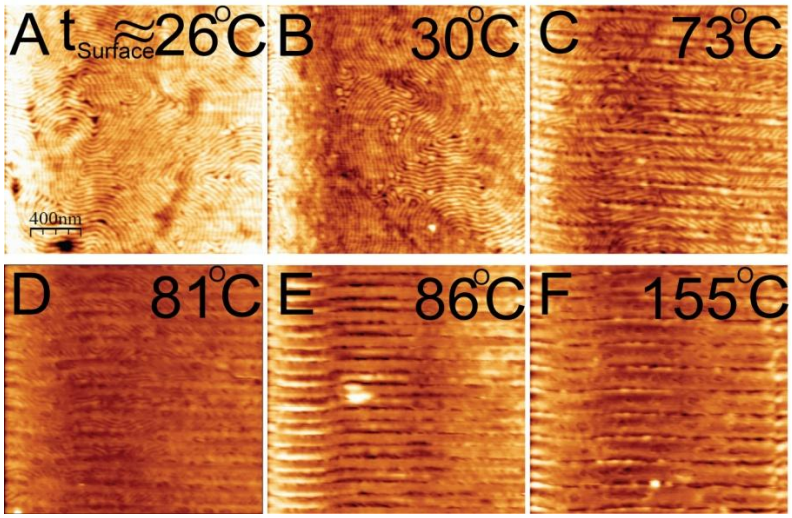

Figure 2.5. Single thermal scans with increased line spacing. 2 μm x 2 μm AFM topographs of a polymer surface after a single scan with a thermal tip over 50 μm x 50 μm areas modified at tip-polymer interface temperatures of: A) 26 ± 7 °C, B) 30 ± 7 °C C) 73 ± 10 °C, D) 81 ± 11 °C, E) 86 ± 11 °C, and F) 155 ± 20 °C.

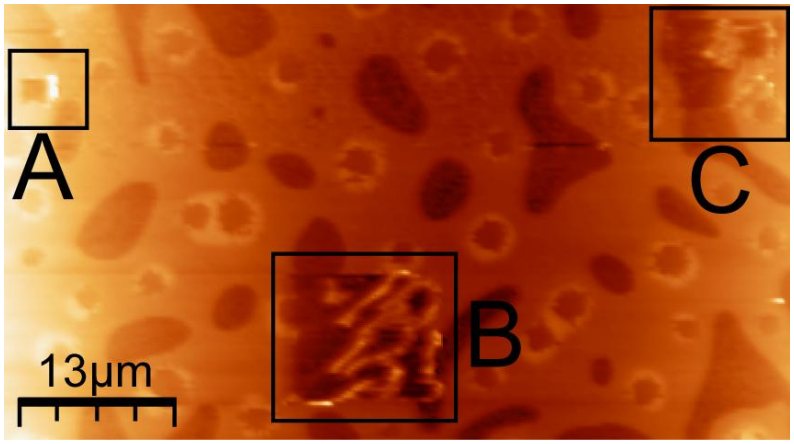

Figure 2.6. High force and heat scans. Various sizes AFM topographs of high force scans (few nN) with a tip heated to 63 ± 10 °C. A) a box with an original 2 μm x 2 μm scan B) a box with a 10 μm x 10 μm scan repeated 3 times C) a box with a 7 μm x 7 μm scan.

2.4. Discussion

2.4.1. Molecular structure of the PS-b-PEO

To explain the results, this section develops a microscopic model of the polymer film. Once PS and PEO segregate into the lamellar phases the equilibrium fingerprint spacing, d_{EQ}, is determined by i) packing constraints and energy for the PEO blocks folding in the crystalline domains and ii) entropic conformational and stretching free energy for the PS blocks in the amorphous domains.[66] Various equilibrium mean field models for these energy contributions were proposed and tested,[66-70] but the mean field theory of Whitmore and Noolandi[66] predicted d_{EQ} specifically for PS-b-PEO copolymers. Whitmore and Noolandi suggested that a given

lamella comprises either one or two stacks of crystalline PEO layers arranged side-by-side shown in Figure 2.7.

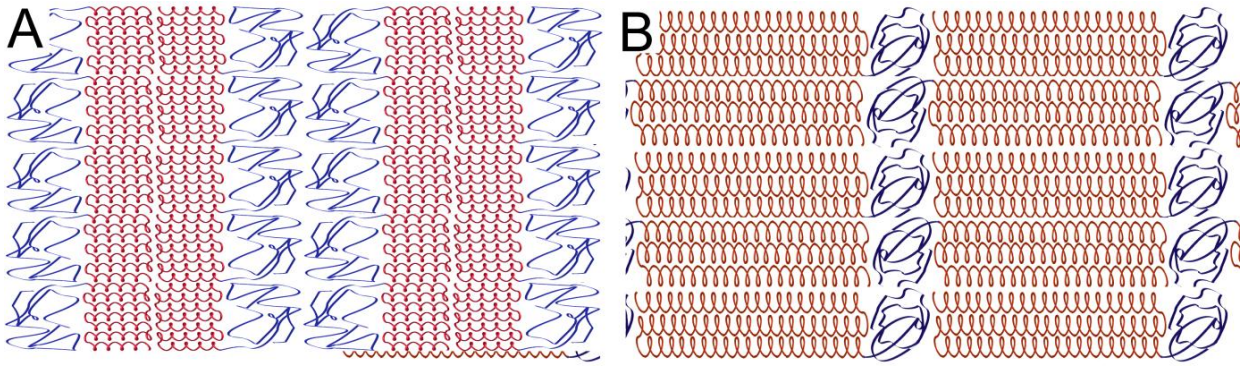

Figure 2.7. Whitmore and Noolandi PS-b-PEO stacks. A) A double stack and B) a single stack arrangement of PS-b-PEO lamellae. According the theory of Whitmore and Noolandi[66] a single stack lamella corresponds closer to the results presented in this work.

By applying their model with the single PEO stack configuration for Z_{PS} = 130 and Z_{PEO} = 350, d_{EQ} = 57.8 ± 9.6 nm and the ratio of d_{PEO} to d_{PS} is 2.7. Appendix B contains the calculations in Mathmatica coding. The calculated value of d_{EQ} is about 40% higher than experimental measurements found with AFM, but mean field theories do not follow experimental data strictly.[71] Possible reasons for inconsistencies are that Whitmore and Noolandi do not include the effects of the surface energy on the PS-b-PEO stack, variations of the free energy of Helmholtz gain per each fold E_{fold} in the crystalline PEO phase,[72] and dependence of d_{EQ} on annealing temperature.[14] Thus, instead of a predicted value of d_{EQ}, the 2.7 ratio of d_{PEO} to d_{PS} is further used to obtain $d_{PEO\_PREDICTED}$ = 28 ± 5 nm and $d_{PS\_PREDICTED}$ = 11 ± 2 nm.

The PEO and PS structures are predicted as follows. PEO crystallizes in the lamellar phase in a 7_2 helix with a pitch ≈1.95 nm.[73] Figure 2.8 approximates that each PEO molecule is parallel to the substrate surface and comprises several folds. The theoretical length of an *n*-folded PEO chain is $d_{PEO\_THEORY} = (1.95/7)Z_{PEO}/(1+n)$. Equating d_{PEO_THEORY} with $d_{PEO\_PREDICTED}$ we get two folds per each PEO chain (n = 2), and an apparent height of the PEO molecule as 3 x 1.95 nm = 6 nm.[74] In a typical lamellar structure, PEO is concentrated in the valleys, and PS in the hills. This was not checked on the sample, *e.g.*, by binding selective markers to the PEO[75] and PS,[76] respectively, but in Figure 2.1A a measured 1 nm difference between the valleys and the hills in lamellas is present. To explain this finding, approximate the PS part of each PS-b-PEO molecule as an ellipse with a longer radius of $d_{PS\_PREDICTED}/2 \approx 5.5$ nm, and a shorter radius x. To find the value of x, equate a volume of such an ellipse with a volume a sphere with the PS

gyration radius, $R_{G,PS}$. The value of $R_{G,PS} = b_{PS} (Z_{PS}/6)^{(1/2)} = 3.2 \pm 0.5$ nm, where $b_{PEO} = 0.7 \pm 0.1$ nm is the PS Kuhn's length.[77] $R_{G,PS}$ in a toluene is 10 – 30% more,[78] so estimate that $R_{G,PS} = 3.8 \pm 0.5$ nm. With the preceding information, $x \approx 3.5$ nm. This also makes the PS component to be about one nm thicker than the PEO cylinder.

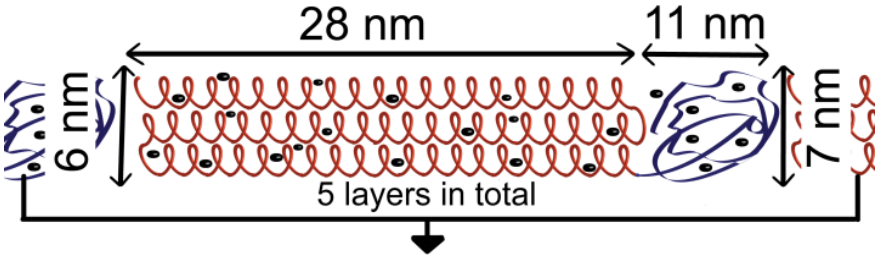

Figure 2.8. Proposed molecular structure of the PS-b-PEO lamella. The PEO chains (28 nm long and 6 nm high) are folded and arranged into one stack with two folds. The PS chains are amorphous, partially stretched along the lamella, and approximated as an ellipse (11 nm long and 7 nm high). The PS-b-PEO film comprises five lamellar layers.

The molecular model in Figure 2.8 implies that lamellae are laterally and vertically connected. For any two lamellar layers on top of each other there is 50% chance that a given PS-b-PEO molecule sits entirely atop just one PS-b-PEO molecule. For five layers in the film, the probability is only $(1/2)^4 = 1/16$ or $\approx 6\%$ for creating long ordered structures, which are easy to disrupt at the interface between neighboring PS-b-PEO molecules. Laterally mixed and vertically "not easy to break through" lamellae are expected to be predominant. A given lamellar arrangement of all five consecutive layers must propagate laterally in the sample, because any single flips of the PS-b-PEO molecules would produce a defective lamella with two PEO stacks, that is, a longer and less thermodynamically stable lamella.

The stepwise thermo/annealing method depends on dewetting, local solvent concentration, temperature, pressure, and material permeation to the solvent,[56, 76, 79] so that local non-equilibrium morphologies are expected. [56, 76, 79-80] Figure 2.1E shows dendritic branches of similar size and with many tip-splitting events. Similar growth pattern was observed in the case of amorphous polymeric nanowires.[81] These observations were explained as diffusion limited aggregation/solidification of amorphous material by Mullins-Sekerka and Gibbs-Thompson effects. Mullins-Sekerka effects relate to dendritic growth of higher surface energy phase and Gibbs-Thompson effects related to dissolving sharp protrusions.[81-84] Strong affinity of the PEO blocks to the Si substrate and higher PEO surface energy than that of the PS block ($\gamma_{PS} \approx 33$ mN m^{-1}, and $\gamma_{PEO} \approx 43$ mN m^{-1})[76] are yet another reasons for the dendrites to be in amorphous or in a very weakly separated state. Only then, the dendrite's height, here: 12 nm, is substantially less

than twice the sum of the gyration radii for the PS and PEO blocks, here: 20 nm ($R_{G,PS}$ = 3.8 ± 0.5 nm and $R_{G,PEO}$ = 6.1 ± 0.7 nm). In contrary, the "bubble" base in Figure 2.1C is smooth and non-dendritic, so likely there was no lack of solute and/or polymer there during an annealing process. One could hypothesize that frayed edges of the bubbles result from fast solvent evaporation producing locally supercooled structures of amorphous PS-b-PEO, which did not crystallize or dewetted due to solvent induced entanglements between the PEO blocks.

2.4.2. Modeling a change from fingerprints to ripples

This section explains observations from Figure 2.2. These are: i) a smear-like, or abrasive, initial topography of the PS-b-PEO sample, ii) an exponential-like growth of ripples with a scan number, iii) saturation of this growth, and iv) a step-like ripple growth thereafter.

The initial abrasive topography of the PS-b-PEO sample originates in the PS and PEO properties. The PS films with $M_{n,\mathrm{PS}}$ of less than 40 kg mol^{-1} are "liquid-like" and not-liking to form ripples.[64-65] Aioke *et al.*[64] and Meyers *et al.*[65] obtained the initial abrasive pattern on PS films, which only after at least 15 consecutive scans started to show some ripples. The PEO films do not like to form ripples either. Leung and Goh[35] were unable to produce ripples on the PEO films on mica despite using a range of contact forces from several nN to 100 nN, which was sufficient to obtain ripples on other polymers.[17, 19, 35, 63-65]

Growth and evolution of ripples were investigated on several amorphous polymers, e.g., on poly(methyl methacrylate), polycarbonate, or polysulfonate.[17, 19, 35, 63-65] Literature models relate the origins and evolution of ripples to polymer properties alone,[65, 85] local cracks formation and subsequent polymer peeling,[86] or wearing the surface during each scan balanced by the surface relaxation.[19, 87] In the case of amorphous polymers ripples align almost perpendicular to the fast scanning direction, which is also observed in Figure 2.2. However, in the case of this sample's PS-b-PEO lamellae, see Figure 2.8, one would expect less surface relaxation, and faster formation of ripples than in the case of amorphous polymers. Then, as in Figure 2.A, the value of λ is dominated by an extensive elasto-plastic deformation of the polymer surface conforming to the shape of a scanning AFM tip to yield:

$$\lambda = 2\sqrt{4RD - D^2} \qquad \textbf{Equation 2.1}$$

Using Equation 2.1and an AFM tip curvature radius of R = 38 ± 5 nm,[88] λ = 39 ± 5 nm for D = 2.5 ± 0.5 nm from Figure 2.2C and λ = 68 ± 6 nm for D = 8 ± 1 nm from Figure 2.2D.

The measured $\lambda \approx 100$ nm in Figure 2.2C and ≈140 nm in Figure 2.2D. Equation 2.1 yields about half of the expected values of λ, so a more detailed model is needed.

To fill this need, a model is developed based on the crack propagation and stick-and-slip of an AFM cantilever. Another model with a lateral crack propagation underneath the sample and resulting polymer peeling was proposed in the literature to explains ripples on amorphous polymers.[86] However, we did not observe peeling on the copolymer sample. Figure 2.B shows that due to wedge-like geometry of an AFM tip indenting the polymer a change from fingerprints to ripples might be understood in terms of a vertical mode I type crack, also known as "tension" or "opening mode",[60] growing upon cyclic loading. During each pass of the AFM tip over a given area, a crack grows till its strain energy release rate, G, surpasses the polymer surface energy w.[60] Using the Dugdale model of a crack growth,[60] the equilibrium value of G is calculated as $G = \delta_t \sigma_0$, where δ_t is the surface opening of a crack, and σ_0 is the crack opening stress. A spherical cap of "$2\pi R(D+H)$" approximates the tip-sample contact area with H being the height of a polymer material pile removed during indentation of the depth D. The crack grows when an AFM tip "sticks" to it. Once mechanical energy stored in the cantilever due to lateral bending of the tip ($0.5\, k_{lat}\, \Delta^2$) exceeds the tip-polymer surface energy over the contact area, the tip "slips" laterally by the distance, Δ, to a new contact point. Thus:

$$G = \delta_t \sigma_o = w = \frac{0.5 k_{lat} \Delta^2}{2\pi R(D+H)} \quad \Delta = \sqrt{\frac{4\pi R(D+H)\delta_t \sigma_o}{k_{lat}}} \qquad \textbf{Equation 2.2}$$

Here, $k_{lat} = 32 \pm 11$ N m^{-1} is the lateral stiffness of the MLCT-D cantilever, which was calculated using the Neumeister and Ducker model.[38, 89] Using the same model, the normal spring constant is 46 ± 3 mN m^{-1}, which is typical for this cantilever.[20, 40] The usual approximation of $\sigma_0 = 1.2\, \sigma$,[60] was used. Where $\sigma = 50$ MPa is an estimated actual stress at the plastic yield point for polymers.[60] Overall, the lateral wavelength of the ripples, λ, becomes:

$$\lambda = \delta_t + \Delta \qquad \textbf{Equation 2.3}$$

Using the values of $R = 38 \pm 5$ nm, $D = 3 \pm 1$ nm, $H = 7 \pm 2$ nm, and $\delta_t = 55 \pm 10$ nm taken along a slow scanning direction from Figure 2.2C and Equation 2.3 wavelength of the ripples becomes, $\lambda = 77 \pm 16$ nm.[90] Such a value of λ is much closer to the experimentally observed 100 nm than the results of Equation 2.1. Furthermore, in the Dugdale model the crack's depth and lateral mouth opening increase upon cycled loading or consecutive scanning according to a power law. This would explain fast and non-linear growth of λ with the scan number.

Saturation of λ resembles the crack growth due to material hardening,[60] but it can also be due to a small thickness of the film, which inherently limits the crack's growth. Finally, the jumps of λ in the saturated region might be due to partial unfolding of the PEO chains, see Figure 2.8. The crack propagation and stick-and-slip model appears to closely represent the experimental data in Figure 2.2.

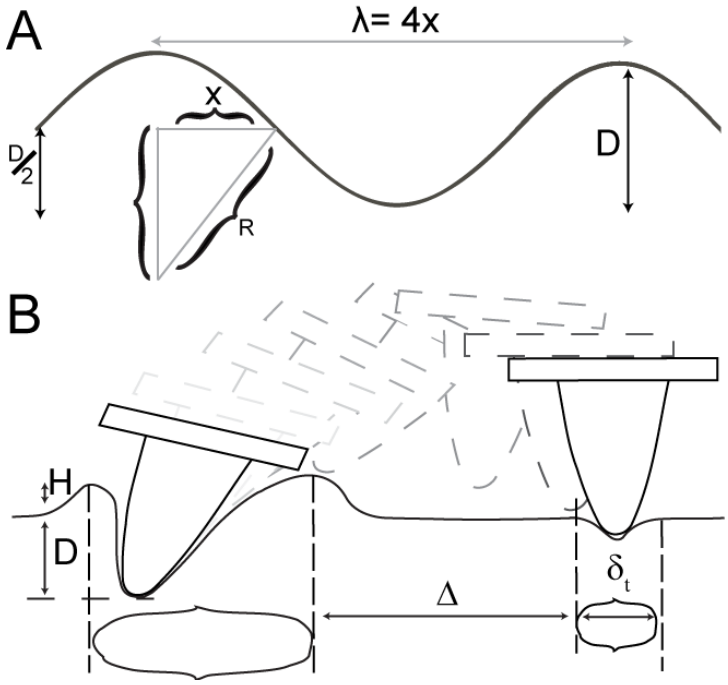

Figure 2.9. Model to explain surface nano-ripples. A) Basic tip-surface indentation model. B) Crack propagation – slip-and-stick model. An AFM tip "sticks" in the crack, opens it by δ_t,[60] and later "slips" a distance Δ to a new location. Scanning over the same area deepens the crack. Bottom drawings are surface profiles of idealized cracks.

2.4.3. Thermal analysis

There are several characteristic temperatures of the PS-b-PEO polymer: the melting temperature, T_m^{PEO}, for the PEO block, the local glass transition, T_g^{PS}, for the PS component, and the order-disorder transition temperature, T_{ODT}, at which symmetric copolymers with lamellar phases transition directly into disordered melts.[77] These temperatures decrease with an increase of the film thickness,[91-93] increase for longer polymer chains,[94] and are lower for copolymers than their components alone or in melts.[95] They depend on a film deposition method,[77] crystallization temperature and speed,[96] film-sample interfacial energy.[48] In AFM-based experiments, T_g^{PS} decrease with increasing the tip-sample contact force,[91-93] and the tip-sample contact time.[97] To estimate these temperatures we compared various studies using calorimetry, X ray scattering, and AFM methods for the PS and PEO components, their melts, and PS-b-PEO copolymers with different $M_{n,\mathrm{PS}}$ and $M_{n,\mathrm{PEO}}$. The estimated values are: T_m^{PEO} between 50 to 60 °C, T_g^{PS} between 60 to 70 °C, and T_{ODT} above 170 °C.

In the following section the T_m^{PEO} and T_g^{PS} are obtained from experimental measurements. Repetitive scanning over the same area at 28 ± 7 °C at tip-surface shown in Figure 2.3B and scanning at 41 ± 8 °C tip-surface temperature shown in Figure 2.4B, produce abrasive patterns seen in the literature for non-melted PS polymers.[64-65] However, the polymer film in Figure 2.4C obtained at 66 ± 10 °C is removed from the surface in chunks. Since contact force in Figure 2.4C is no larger than in Figure 2.4A-B, this implies that both melting and glass transition must have occurred between 41 °C and 66 °C. The T_g^{PS} estimate is only marginally larger than the T_m^{PEO} estimate, so within the experimental error these two temperatures are expected to fall within 54 ± 12 °C. The time-temperature superposition principle[97] applied to Figure 2.4C and Figure 2.5C confirms the PS glass transition temperature at 54 ± 12 °C. Figure 2.5C shows first visible plastic indentation lines while scanning (50 μm/s) / (1.7 μm/s) ≈ 30 times faster than in Figure 2.4C. Then, $a_T = \tau/\tau_{REF} = 30$ is the time-temperature superposition shift factor, where τ is the time scale of a glass transition temperature at a temperature T from Figure 2.4C, and τ_{REF} is the respective time scale associated with a glass transition temperature at a reference temperature, T_{REF} = 73 ± 10 °C from Figure 2.5C. The value of T is obtained from the Williams-Landel-Ferry equation:[97]

$$T = \frac{T_{REF}\left(\log a_T - C_1\right) - C_2 \log a_T}{\log a_T + C_1} \qquad \textbf{Equation 2.4}$$

where C_1 and C_2 are material constants at T_{REF}. Using C_1 = 13.6 and C_2 = 51 °C obtained for bulk PS at 100°C,[98] we get T = 67 ± 10 °C. This estimate might not strictly apply here, but the value of T = 67 ± 10 °C compares well with the temperature of 66 ± 10 °C in Figure 2.4C.

The following is a comment about the T_{ODT}. The data in Figure 2.4D was obtained above T_g^{PS} and T_m^{PEO}. At these conditions, as marked by a 30 nm deep cross-section on an inset of Figure 2.4D, the thermal tip removed all of the polymer film from the surface. This suggests melting and/or softening over a whole thickness of the polymer film, which agrees with the thermal analysis below. However, after melting amorphous polymer is not expected to get entirely removed from the surface due to some plowing through the material. Increasing the temperature did not produce plowing effects either. Similarly, it is difficult to distinguish pure plowing at a larger imaging scale in Figure 2.5. Therefore, both on small and large AFM imaging scales one could not conclusively observe any order-disorder transition.

The number of molecules affected mechanically at $T_g^{PS} \sim T_m^{PEO}$ is found next. Elastic contact mechanics fails for large indentations expected in the vicinity of T_m^{PEO} and T_g^{PS}. At these

temperatures the tip-sample contact radius *a* estimate is directly from the convolution with a tip profile in Figure 2.5C to get $a = 19 \pm 3$ nm.[99] Contact mechanics predicts that vertical stresses in the sample vanish at indentation of more than *3a*, and that the lines of equal pressure form a "semi-bone" shape as Figure 2.10A.[60] Thus, in the vicinity of T_m^{PEO} and T_g^{PS}, mechanical force affects the entire 30 nm thickness of the polymer film. To obtain the mechanically affected volume approximate it as a hemi-ellipse with a minor radius of 19 nm ± 3 nm and a major radius of 30 nm, which yields ≈22,700 nm^3. A volume of 39 x 7 x 6 nm^3 for each PS-b-PEO molecule, see Figure 2.8, yields 13 PS-b-PEO mechanically affected molecules.

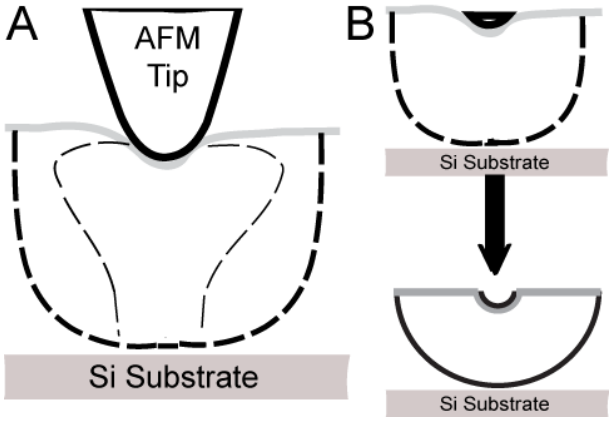

Figure 2.10. Thermal and mechanical affected contours. A) Thermally (outer semi-ellipse contour) and mechanically (inside semi-bone contour) affected zones at the onset of PEO melting and PS softening. B) Thermally affected zones are substituted by equivalent hemi-spheres for calculations of the heat flow using Equation 2.5.

To find how many molecules are affected thermally at $T_g^{PS} \sim T_m^{PEO}$; find the thermal isotherm, I_T, kept at $T_m^{PEO} \approx T_g^{PS} = 54 \pm 12$ °C, i.e., encompassing a polymer volume beyond which no significant melting/softening happens. A good estimate of I_T is so-called the "critical core" isotherm reaching down to the Si substrate. This is because the polymer film is very thin, so the Si substrate is a potent heat sink,[100] which absorbs heat and limits any further growth of the melting/glass transition zone. The critical core isotherm estimate comes from finite element modeling in Ref.[43], yielding that I_T is a hemi-ellipse with major radius being the film thickness (30 ± 2 nm), and a minor radius of 22.5 ± 3 nm, see Figure 2.8A.[101] The critical core volume is 31,800 nm^3. The tip-sample contact in Figure 2.5C is a 5 nm deep spherical cap with a contact radius of 19 ± 3 nm, and a volume 2850 nm^3. The difference of these respective volumes is 29,000 nm^3, which corresponds to 17 thermally affected PS-b-PEO molecules, and 30 attograms of the polymer.

Knowing the mechanically and thermally affected volumes and number of molecules several thermophysical parameters can be calculated as follows. Figure 2.10B shows how to obtain the heat flux, *q*, which flows from the AFM tip into an area bound by the isotherm I_T, by calculating it between two hemispheres defined to match the respective volumes of the tip-

surface contacting spherical cap and the critical core zone.[59] The spherical cap is substituted by an equivalent hemisphere with the radius R_{in} = 11 ± 1 nm, and the elliptical critical core cap is substituted by an equivalent hemisphere with the radius R_{out} = 25 ± 1 nm. Yeilding:[59]

$$q = \frac{2\pi k R_{in} R_{out} \Delta T}{R_{out} - R_{in}} = 0.36 \pm 0.12 \mu W \qquad \textbf{Equation 2.5}$$

where: k = 0.15 ± 0.01 W $K^{-1}m^{-1}$ is the polymer conductivity estimated from Ref.[18], and ΔT = 73 °C - 54 °C = 19 ± 12 °C.

Knowing q, one can estimate the local specific heat C_p as $C_p = Q/[(\Delta m)\ (\Delta T)]$, where: $Q = qt$ is the heat delivered in the time, t, to the thermally affected mass Δm within I_T in order to raise its temperature by ΔT. One would evaluate t from the time an AFM tip resides at a contact radius a, so that $t = a/\upsilon$, where υ is the scanning speed. However, one should rather use the time, t_s, it takes to establish the temperate gradient, and consequently a steady-state heat flow.[18, 57] Derivations in Ref.[18] yield $t_s \approx 6 \pm 1$ ns for 30 nm thick polymer film, so that C_p = 3.6 ± 2.7 J $g^{-1}K^{-1}$. Such a value of C_p matches very well typical values for polymers. Then, the PEO melting enthalpy, ΔH_{melt}, is obtained as $\Delta H_{melt} = C_p\ (T_m^{PEO} - T_{room}) = 111 \pm 88$ J g^{-1}, where T_{room} is the room temperature estimated at 23 ± 1 °C. This value of ΔH_{melt} matches the PEO melting enthalpies of 50 to 150 J g^{-1} obtained using calorimetric methods[95] in the case of the PEO block copolymers with PMA. Finally, taking into account that PEO melting affects about 17 PS-b-PEO molecules, the melting enthalpy per each PEO molecule is $\Delta H_{melt}/17 \approx (2 \pm 1) \times 10^{-16}$ J**.** Calculating an apparent "surface" of each PEO molecule, and accounting on three pieces of the crystalline PEO within each PS-b-PEO molecule, the molecular free energy of Helmholtz estimate for unfolding (and melting) of a PEO component with the PS-b-PEO molecule, which is of the order $\approx 10^{-20}$ J nm^{-2}. Such calculations must be treated cautiously, the value $\approx 10^{-20}$ J nm^{-2} is of the same order of magnitude as E_{fold} used in the mean field theories of Whitmore and Noolandi.[66] Furthermore, the molecular free energy of Helmholtz estimate for unfolding (and melting) of PEO compares with AFM estimates on globally melted PEO films.[94]

2.5. Conclusions

This chapter has explained the thermomechanical response of an ultrathin film of the PS-b-PEO polymer to a local force and heat using elasto-plastic contact mechanics and heat flow models. Combining the Dugdale model of crack formation with the stick-and-slip behavior of the AFM tip explained how the fingerprints develop into ripples. Several thermophysical properties

of the copolymer film have been calculated using analytical models and results of the finite element modeling. These values are: C_p = 3.6 ± 2.7 J $g^{-1}K^{-1}$, ΔH_{melt} = 111 ± 88 J g^{-1}, and molecular free energy of Helmholtz for the PEO within the PS-b-PEO molecule at volumes comprising 30 attograms of a polymer material. Also, good lateral connectivity within copolymer layers and easiness to form surface ripples are the limited factors, which prevented inducing alignment of the fingerprint pattern over microscopic length scales. Small free molecular surface energy of the PEO melting and close proximity of T_g^{PS} to T_m^{PEO} produces excessive disorder in the locally heated polymer film. This additionally hinders thermally induced alignment of the fingerprint pattern. Thinner copolymer films are less laterally connected, but are not expected to work either, since both melting and softening temperature decrease with the film thickness. Suggestions to possibly achieve thermally induced alignment are better separation between PEO melting and PS softening and increased interactions between PS-PS and/or PEO-PEO. This might result in using higher molecular weight block copolymers. Such polymers, however, would have larger lamellar periodicity, which is not a preferred strategy. Lastly, another approach is to use asymmetric block copolymers.

Chapter 3- Velocity Dependence of Nano-Abrasive Wear Obtained Using a Spiral Scan Pattern

The work in this chapter has been done in collaboration between Reginald H. Rice and Dr. Robert Szoszkiewicz with Dr. Enrico Gnecco and Dr. Reinhold Wannemacher. Drs. Gnecco and Wannemacher are with Instituto Madrileño de Estudios Avanzados en Nanociencia,Campus Universitario de Cantoblanco, Madrid, Spain. Both collaborators provided ideas, help to explain the observed phenomena, and provided valuable corrections to communicate findings clearly. Thermal levers used in this chapter were again provided by Dr. William P. King.

3.1. Introduction

One of the most interesting, but less exploited features of AFM is its capability of locally modifying the morphology of a surface and tracking its variations before, after, and during the modification process. For instance, periodic ripple patterns can be formed on polymers[31, 35], metals[39], ionic crystals[39] and semiconductors[102] if the probing tip of an AFM repeatedly scans back and forth on these surfaces with a normal pressure exceeding the yield strength of the material. Polymers can also be patterned with a single scan line when the temperature of the contact region exceeds the glass transition temperature of the sample[91].

In most experimental investigations, the scan path of the probing tip is the same as the one usually adopted for imaging the sample surface, i.e. zigzag or raster scanning on a square area. However, while the scanning pattern does not play an important role for imaging, the situation is very deferent when the surface is worn out by the tip. In a recent study, `traveling' ripples have indeed been observed when a circular track is continuously scanned[19]. In this case one can measure the `group velocity' of the ripples and relate it to the wear rate of the material. This chapter's focus is on a deferent shape, i.e. an Archimedean spiral, and takes advantage of its geometric properties to study the abrasive response of polymers at temperatures elevated locally at the tip-sample interface. In this way, a single AFM image acquired after scratching the polymer surface can provide important information for a quantitative characterization of the velocity dependence in nano-wear processes with applications in NEMS, MEMS as well as polymer coatings.

3.2. Materials and methods

The polymers used in this chapter are PMMA and PS polymers from American Polymer Standards Corporation, with number average molecular weight $M_{w,PS}$ = 215.7 kg mol^{-1} and M_w; PMMA = 120 kg mol^{-1}, and polymer polydispersity 1.1. Both films were produced with methods discussed in Chapter 1.2. and preparation steps for PS are detailed in Appendix D. The PMMA film was prepared just as PS except chloroform from Sigma-Aldrich was used as the solvent and the PMMA was annealed 15.5 h at 55 °C followed by 1 h at 90 °C.

The AFM topographs of polymer films were recorded in contact mode with the di-CP-II AFM system, photographed in Figure 1.7, Proscan software, and SiN_x MLCT-D cantilevers, see Figure 1.2A. The MLCT-D cantilevers had a nominal elastic spring constant between 0.04 to 0.07 N/m and nominal curvature radii below 20 nm. For scanning at various tip-sample temperatures the HT-AFM set up in discussed in Chapter 1.1.3 was mounted in the di-CP-II. The tip temperature calibration was based on methods covered in Appendix A and the elastic spring constants of the cantilevers found with techniques in Chapter 1.1.4. From the SEM (see Figure 3.4) the radius of curvature of the tip apex in the transverse direction (R_x = 120±10 nm) is significantly smaller than the longitudinal radius (R_y = 170±10 nm).

3.3. Results

Assuming that the radial distance r of the spiral grows linearly with the time t as r(t) = At, and that the angular velocity ω is constant, it is easy to see that the linear velocity v of the probing tip grows with r as $v = \sqrt{(A^2 + (\omega r)^2)}$. This dependence becomes almost linear, and the velocity almost tangential, when $r \gg A/\omega$, which is the case for all spiral windings in this experiment, except the very first one.

Figure 3.1A shows a representative AFM topograph of a spiral generated on the PS sample at 206 °C on the cantilever, which corresponds to 97 ± 12 °C on the tip-sample interface. A cross section profile is shown in Figure 3.1B. Note that in the first windings the material pushed aside of the groove partially overlaps, whereas this is not the case after the eighth revolution of the tip around the spiral center. In any case, the amplitude of the indentation profile dramatically decreases with the scan speed. Intuitively, this can be understood as follows. The longer the tip keeps indenting a given spot on the surface, the more damage is caused, so that the amplitude is expected to decay with v. To explore this assumption the corrugation as a function of the scan velocity was plotted (Figure 3.2). In a previous AFM analysis on abrasive nanowear

of alkali halides[32] researchers found that the wear rate decreases exponentially with the `time of residence' spent by the tip at a given location on the surface. A similar assumption was proposed by Mulhearn and Samuels to interpret the abrasion of steel sliding against silicon carbide paper[103]. Since in the present case the time of residence is inversely proportional to the scan velocity, the data points in Figure 3.2 have been fitted with the following function:

$$h(v) = h_o\left[1-\exp(-\frac{v_o}{v})\right] \qquad \textbf{Equation 3.1}$$

As shown by the continuous curve in Figure 3.2, an excellent agreement is found when h_0 = 209±10 nm and v_0 = 6.0±0.4 μm/s. In Equation 3.1the parameter h_0 corresponds to the indentation depth of the sample at a given load, when the tip is not driven along the surface, whereas the parameter v_0 quantifies how fast the wear damage decays with the linear speed.

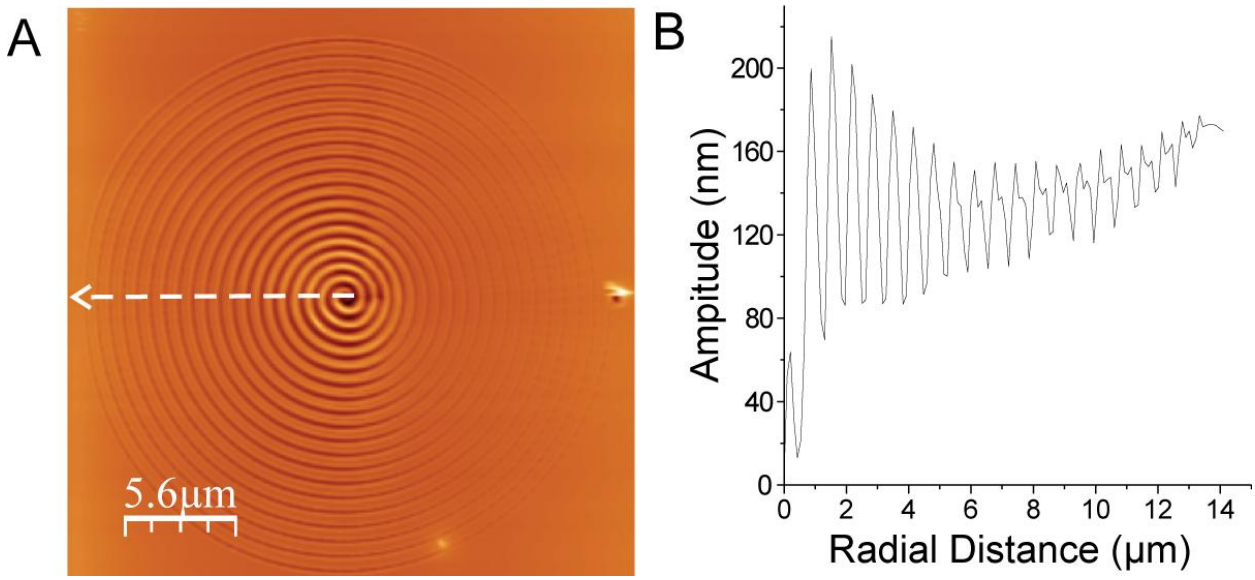

Figure 3.1. Archimedean spiral with azimuthal cross section. A) An Archimedean spiral on PS made with a hot-tip AFM with a normal force F_N = 10 ± 3 nN and an angular velocity ω = 3.14 s^{-1}. This topography rescan (frame size: 28 μm) was obtained with a regular contact mode AFM using MLCT-D lever from Bruker at load of 2±1 nN. Note the deep pit at the end of the spiral, where the tip motion is stopped. B) A cross section along the dashed lines in A.

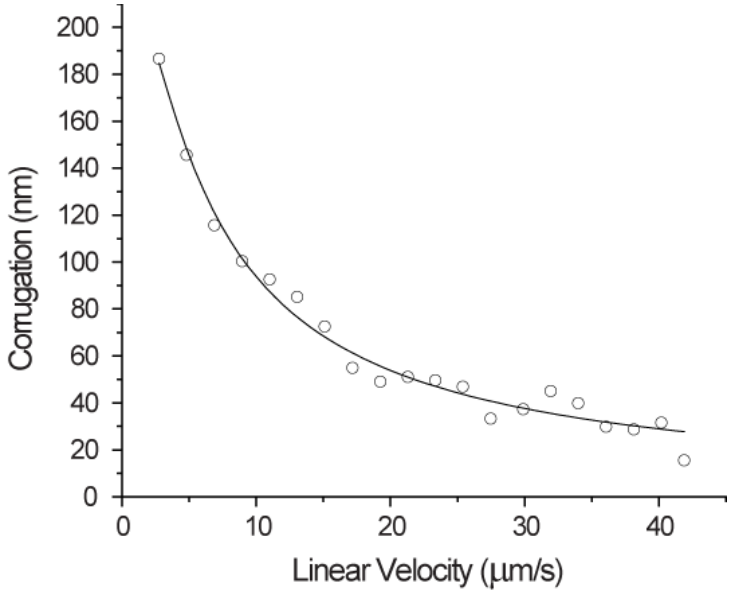

Figure 3.2. Corrugation profile. Corrugation profile obtained from Figure 3.1B by subtracting the maximum height of the material pushed aside from the indentation depth of each groove along the profile. Corrugation profile is plotted by **Equation 3.1** with h_0 = 209 ±10 nm and v_0 = 6.0 ± 0.4 μm/s.

This analysis is extended to other spirals obtained in the PMMA and PS samples at different conditions. In particular, a range of temperatures around the glass transition has been explored, which occurs at 95 ± 5 °C and 105 ± 5 °C for the PS and PMMA samples respectively. The limit value h_0 was always in the range of 100 nm, i.e. comparable to the obtained corrugations, whereas the 'decay velocity' v_0 remained on the order of 10 μm/s in the series of measurements performed. However, the values of both quantities exhibit significant scattering. This is not surprising, since the roughening rate of polymers on the nanoscale has been reported to peak up and scatter in the region of T_g[104]. Even more scattered are the values for the 'decay velocity' v_0, which was found to vary between 1.8 and 20 μm/s in the series of measurements performed.

Two extreme cases, corresponding to v_0 = 5±1 μm/s and 0.6±0.2 μm/s respectively, are showed in Figure 3.3A and B. The spiral in Figure 3.3A was obtained on PMMA at 97 ± 12 °C. In this case the corrugation did not decrease significantly after the first windings, as if the material opposed almost no resistance to dragging. This is not the case for the spiral in Figure 3.3B, the amplitude of which quickly decayed after only two revolutions. However, this spiral was produced at lower temperature of 89 ± 12 °C at the tip-sample interface, which is below the glass transition of PMMA. One should also note that the indentation patterns along each winding are not varying uniformly, but undulate, which is presumably related to the elongated shape of the tip apex.

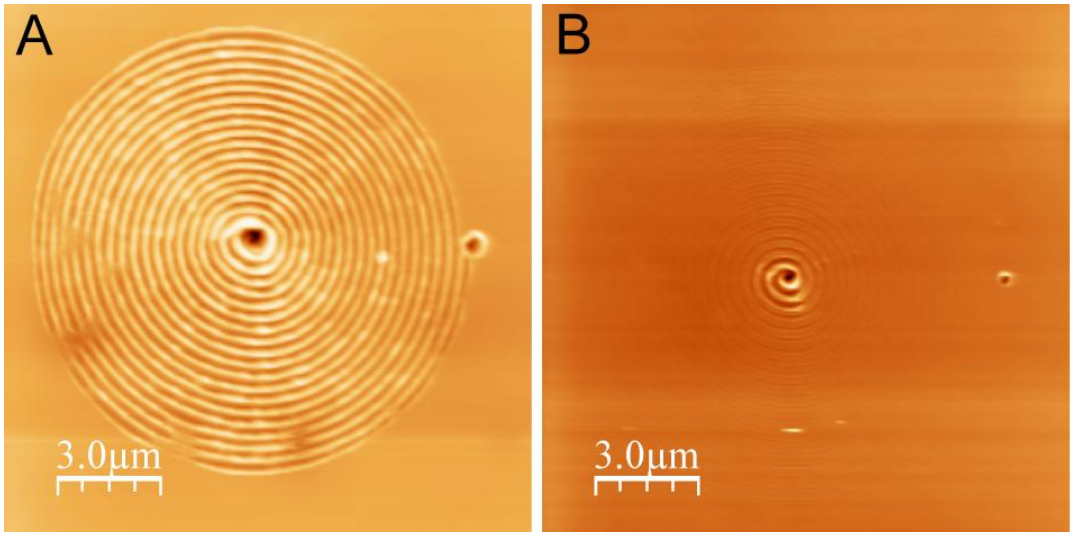

Figure 3.3. Variations in nano-plowing near Tg. As the glass transition temperature is approached, the response of a polymer surface to nano-plowing can be quite variable. This is shown in the case of two spirals made on an initially at PMMA surface A) at 97 ± 12 °C and B)at 89 ±12 °C. Frame sizes: 15 μm.

To investigate this claim further, the thermal tip used in this study was imaged with SEM and analysis details are presented in Figure 3.4. Figure 3.4B shows that its radius of curvature is much smaller along the transverse direction then along the longitudinal direction. This should contribute to less surface heating along horizontal scanning, and higher molds and mountains in the vertical scanning direction.

Examining Figure 3.4A and C an additional structure on the tip side of the cantilever is present. One might get an impression the structure or "other tip" will touch the surface during making of the spirals either contributing to or causing the undulation of indentation patterns. First, no observation of any eccentrically overlapping spirals was noticed. Second, using the presented data, calculated below the other tip is not expected to touch the surface for typical indentations of few hundreds of nanometers. In fact, the "other tip" is ~ 7 μm from the actual tip in Figure 3.4A, and it appears ~200 nm higher than the actual tip in Figure 3.4C. However, Figure 3.4C is tilted in such a way that the cantilever's width of about 10 μm shows there as 1 μm height. Thus, using similar triangles, the height of the other tip in Figure 3.4C needs to be diminished by 0.7 μm. This effectively places the other tip 500 nm below the actual tip. When producing the spirals the cantilever is tilted in a way that increases the vertical distance between the actual and the other tip further.

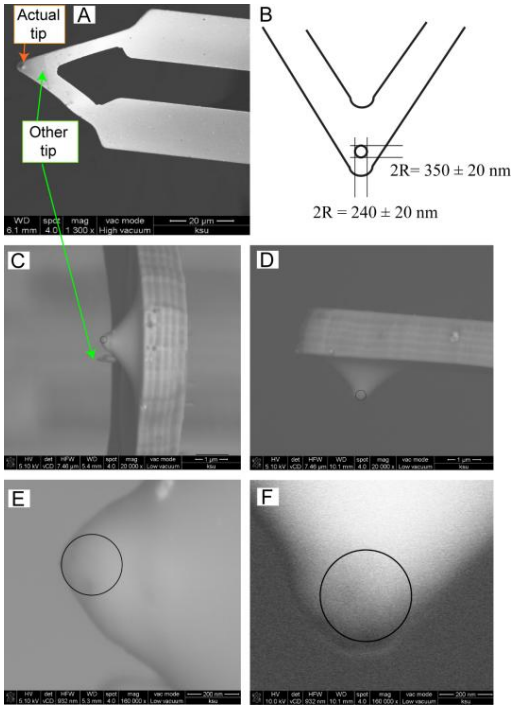

Figure 3.4. SEM images of the thermal tip. This tip produced all spirals presented in this chapter. A) Bird's view of the cantilever with the tip as well as another structure, which shows up at C), but is too low and too far from the actual tip to influence the scans B) The tip curvature radii, which are measured along two perpendicular directions in C)-F). SEM images were taken by Dr. Dan Boyle at the Biology Research Microscope and Image Processing Facility, Kansas State University.

On the other side, since the different spring constants of the cantilever in the x and y directions do not influence the contact stiffness responsible for friction (and wear) on the sample surface[105], the torsional and bending deformations of the cantilever seem not to have a major influence on the spiral patterning.

Finally, the experiments resulted in the formation of ripples inside all spiral tracks. An example is given in Figure 3.5, showing the surface profile in the bottom of a spiral. The ripples are aligned along the radii, which means that their periodicity is proportional to the radial distance r as well as to the scan velocity v. The ripple wavelengths are comparable to previous results of ripples produced in circular scanning in the vicinity of the glass transition temperature on PMMA[19] at corresponding velocities. Although the ripples are seen along the whole spiral, they are more pronounced in two quadrants. This is related to the asymmetry of the indentation patterns along windings previously discussed.

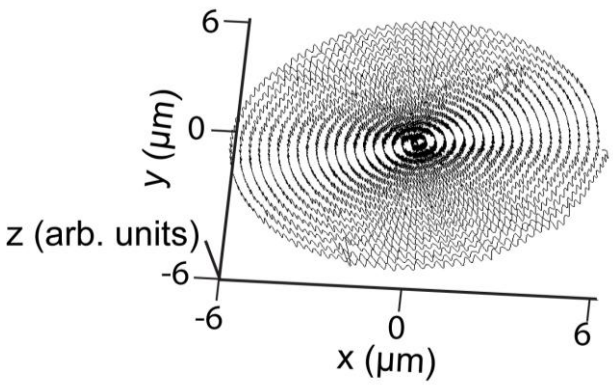

Figure 3.5. Nano-ripples in the spiral grove. Occurrence of surface ripples along a spiral groove. The undulation is enhanced in the second and fourth quadrant of the xy plane compared to the first and third one.

3.4. Conclusions

In conclusion, this chapter has introduced a simple method to characterize the velocity dependence of the wear rate on polymer surfaces. The surface is first scanned by contact AFM adopting a spiral pattern, the damaged area is then rescanned using a ‘standard’ raster pattern and the surface corrugation is finally extracted using azimuthal profiles along the spiral and fitted with an exponential decay law. This method can be extended to other materials, provided that they are brittle enough to be damaged within a single scan. Quantitative information for modeling abrasive wear on the nanoscale can thus be provided by this kind of measurement.

Chapter 4- General Conclusions

This thesis has explored the thermal and mechanical properties of a diblock copolymer, poly(styrene)-b-poly(ethylene oxide), and wear properties of poly(methyl methacrylate) and poly(styrene) thin films. The experiments conducted allowed development of a model explaining PS-b-PEO's lamellar geometry development to ripples. Additionally, measurements provided information to calculate thermophysical properties of the PS-b-PEO. These properties are local specific heat, PEO melting enthalpy and molecular free energy of Helmholtz for the PEO within the PS-b-PEO molecule at volumes comprising of a few tens of attograms of the material. Lastly, a simple method to investigate thin film wear properties to obtain quantitative information for modeling abrasive wear on the nanoscale is presented.

Accomplishment of this was achieved with AFM and HT-AFM methods combined with computer hardware and software to conduct the experiments and record measurements. The information obtained led to the combination of the Dugdale model of crack formation with the stick-and-slip behavior of the AFM tip to model the PS-b-PEO fingerprint to ripple transformation. With analytical models and results of finite element modeling measurements allowed for the calculation the PEO melting enthalpy, 111 ± 88 J g^{-1}, local specific heat, 3.6 ± 2.7 J $g^{-1}K^{-1}$, and molecular free energy of Helmholtz, 10^{-20} J nm^{-2}, for the PEO within PS-b-PEO at volumes comprising 30 attograms of a polymer material The Archimedean spiral scan pattern provided advantages to investigate the velocity dependence of wear of thin PS and PMMA films at locally elevated temperatures. This advantage allowed for development of an exponential decay law for modeling abrasive wear.

Properties of polymer thin films importance are contingent on technological development. Technology continues to shrink in size, thus investigations into the properties of polymer thin films will continue to be critical. This thesis demonstrated that many properties, specifically thermal, mechanical, and velocity dependant wear properties can be examined through simple methods using AFM.

4.1. Future Work

Verification of the models proposed in this thesis over a wider range of variables is of utmost importance. Currently experiments are being conducted to investigate wear of thin polymer films as a function of force, scan speed, scan geometry and cantilever tip radius. This

may also allow new insight into proper choices of cantilever for specific applications. Additionally, data collected during experiments in Chapter 3 are being further analyzed to investigate tip radius effects on velocity dependant wear of thin polymer films.

Future work also needs to be dedicated to improving the accuracy of thermal cantilever tip and tip-surface interface temperature. The error in these temperatures can be significant, near 50%, and a device to directly measure these quantities is currently out of technology's reach. With modeling improvements or a device to directly measure tip and tip-surface interface temperature the accuracy of HT-AFM will improve significantly.

References

1. Segalman, R. A., Patterning with block copolymer thin films. *Mat. Sci. Eng. R* **2005,** *48* (6), 191-226.

2. Kim, H. C.; Park, S. M.; Hinsberg, W. D., Block Copolymer Based Nanostructures: Materials, Processes, and Applications to Electronics. *Chemical Reviews* **2010,** *110* (1), 146-177.

3. Lin, D. Z.; Cheng, T. D.; Chang, C. K.; Yeh, J. T.; Liu, J. M.; Yeh, C. S.; Lee, C. K., Directional light beaming control by a subwavelength asymmetric surface structure. *Optics Express* **2007,** *15* (5), 2585-2591.

4. Norman, J.; Desai, T., Methods for fabrication of nanoscale topography for tissue engineering scaffolds. *Annals of Biomedical Engineering* **2006,** *34* (1), 89-101.

5. Fasolka, M. J.; Banerjee, P.; Mayes, A. M.; Pickett, G.; Balazs, A. C., Morphology of ultrathin supported diblock copolymer films: Theory and experiment. *Macromolecules* **2000,** *33* (15), 5702-5712.

6. Tang, C. B.; Tracz, A.; Kruk, M.; Zhang, R.; Smilgies, D. M.; Matyjaszewski, K.; Kowalewski, T., Long-range ordered thin films of block copolymers prepared by zone-casting and their thermal conversion into ordered nanostructured carbon. *Journal of the American Chemical Society* **2005,** *127* (19), 6918-6919.

7. Stoykovich, M. P.; Muller, M.; Kim, S. O.; Solak, H. H.; Edwards, E. W.; de Pablo, J. J.; Nealey, P. F., Directed assembly of block copolymer blends into nonregular device-oriented structures. *Science* **2005,** *308* (5727), 1442-1446.

8. Darling, S. B., Directing the self-assembly of block copolymers. *Progress in Polymer Science* **2007,** *32* (10), 1152-1204.

9. Cheng, J. Y.; Ross, C. A.; Smith, H. I.; Thomas, E. L., Templated self-assembly of block copolymers: Top-down helps bottom-up. *Advanced Materials* **2006,** *18* (19), 2505-2521.

10. Cheng, J. Y.; Mayes, A. M.; Ross, C. A., Nanostructure engineering by templated self-assembly of block copolymers. *Nature Materials* **2004,** *3* (11), 823-828.

11. Thurn-Albrecht, T.; Schotter, J.; Kastle, C. A.; Emley, N.; Shibauchi, T.; Krusin-Elbaum, L.; Guarini, K.; Black, C. T.; Tuominen, M. T.; Russell, T. P., Ultrahigh-density nanowire arrays grown in self-assembled diblock copolymer templates. *Science* **2000,** *290* (5499), 2126-2129.

12. Angelescu, D. E.; Waller, J. H.; Adamson, D. H.; Deshpande, P.; Chou, S. Y.; Register, R. A.; Chaikin, P. M., Macroscopic orientation of block copolymer cylinders in single-layer films by shearing. *Advanced Materials* **2004,** *16* (19), 1736-1741.

13. Hashimoto, T.; Bodycomb, J.; Funaki, Y.; Kimishima, K., The effect of temperature gradient on the microdomain orientation of diblock copolymers undergoing an order-disorder transition. *Macromolecules* **1999,** *32* (3), 952-954.

14. Ruiz, R.; Ruiz, N.; Zhang, Y.; Sandstrom, R. L.; Black, C. T., Local defectivity control of 2D self-assembled block copolymer patterns. *Advanced Materials* **2007,** *19* (16), 2157-2162.

15. Sundrani, D.; Darling, S. B.; Sibener, S. J., Guiding polymers to perfection: Macroscopic alignment of nanoscale domains. *Nano Letters* **2004,** *4* (2), 273-276.

16. Hong, S. W.; Huh, J.; Gu, X. D.; Lee, D. H.; Jo, W. H.; Park, S.; Xu, T.; Russell, T. P., Unidirectionally aligned line patterns driven by entropic effects on faceted surfaces. *Proceedings of the National Academy of Sciences of the United States of America* **2012,** *109* (5), 1402-1406.

17. Gotsmann, B.; Durig, U., Thermally activated nanowear modes of a polymer surface induced by a heated tip. *Langmuir* **2004,** *20* (4), 1495-1500.

18. Szoszkiewicz, R.; Okada, T.; Jones, S. C.; Li, T. D.; King, W. P.; Marder, S. R.; Riedo, E., High-speed, sub-15 nm feature size thermochemical nanolithography. *Nano Letters* **2007,** *7* (4), 1064-1069.

19. Gnecco, E.; Riedo, E.; King, W. P.; Marder, S. R.; Szoszkiewicz, R., Linear ripples and traveling circular ripples produced on polymers by thermal AFM probes. *Phys. Rev. B* **2009,** *79* (23).

20. Dey, A.; Szoszkiewicz, R., Complete noise analysis of a simple force spectroscopy AFM setup and its applications to study nanomechanics of mammalian Notch 1 protein. *Nanotechnology* **2012,** *23* (17), 175101.

21. Cai, K. Y.; Muller, M.; Bossert, J.; Rechtenbach, A.; Jandt, K. D., Surface structure and composition of flat titanium thin films as a function of film thickness and evaporation rate. *Appl. Surf. Sci.* **2005,** *250* (1-4), 252-267.

22. Walther, F.; Heckl, W. M.; Stark, R. W., Evaluation of nanoscale roughness measurements on a plasma treated SU-8 polymer surface by atomic force microscopy. *Appl. Surf. Sci.* **2008,** *254* (22), 7290-7295.

23. Yu, E. T., Nanoscale characterization of semiconductor materials and devices using scanning probe techniques. *Mat. Sci. Eng. R* **1996,** *17* (4-5), 147-206.

24. Binnig, G.; Quate, C. F.; Gerber, C., Atomic Force Microscope. *Phys. Rev. Lett.* **1986,** *56* (9), 930-933.

25. Eaton, P.; West, P., *Atomic Force Microscopy*. 2nd ed.; Oxford University Press: New York, 2010; p 248.

26. Abdelhady, H. G.; Allen, S.; Ebbens, S. J.; Madden, C.; Patel, N.; Roberts, C. J.; Zhang, J. X., Towards nanoscale metrology for biomolecular imaging by atomic force microscopy. *Nanotechnology* **2005,** *16* (6), 966-973.

27. Doron, A.; Joselevich, E.; Schlittner, A.; Willner, I., AFM characterization of the structure of Au-colloid monolayers and their chemical etching. *Thin Solid Films* **1999,** *340* (1-2), 183-188.

28. Eaton, P.; Ragusa, A.; Clavel, C.; Rojas, C. T.; Graham, P.; Duran, R. V.; Penades, S., Glyconanoparticle-DNA interactions: An atomic force microscopy study. *IEEE Transactions on Nanobioscience* **2007,** *6* (4), 309-318.

29. Gross, L.; Mohn, F.; Moll, N.; Schuler, S.; Criado, A.; Guitián, E.; Peña, D.; Gourdon, A.; Meyer, E.; , Bond-Order Discrimination by Atomic Force Microscopy. *Science* 14 September 2012, 2012, pp 1265-1424

30. Hinz, M.; Kleiner, A.; Hild, S.; Marti, O.; Durig, U.; Gotsmann, B.; Drechsler, U.; Albrecht, T. R.; Vettiger, P., Temperature dependent nano indentation of thin polymer films with the scanning force microscope. *European Polymer Journal* **2004,** *40* (5), 957-964.

31. Elkaakour, Z.; Aime, J. P.; Bouhacina, T.; Odin, C.; Masuda, T., Bundle Formation of Polymers with an Atomic-Force Microscope in Contact Mode – a Friction Versus Peeling Process. *Phys. Rev. Lett.* **1994,** *73* (24), 3231-3234.

32. Gnecco, E.; Bennewitz, R.; Meyer, E., Abrasive wear on the atomic scale. *Phys. Rev. Lett.* **2002,** *88* (21).

33. Hutter, J. L.; Bechhoefer, J., Calibration of Atomic-Force Microscope Tips (Vol 64, Pg 1868, 1993). *Rev. Sci. Instrum.* **1993,** *64* (11), 3342-3342.

34. King, W. P.; Kenny, T. W.; Goodson, K. E.; Cross, G.; Despont, M.; Durig, U.; Rothuizen, H.; Binnig, G. K.; Vettiger, P., Atomic force microscope cantilevers for combined thermomechanical data writing and reading. *Appl. Phys. Lett.* **2001,** *78* (9), 1300-1302.

35. Leung, O. M.; Goh, M. C., Orientational Ordering of Polymers by Atomic Force Microscope Tip-Surface Interaction. *Science* **1992,** *255* (5040), 64-66.

36. Levy, R.; Maaloum, M., Measuring the spring constant of atomic force microscope cantilevers: thermal fluctuations and other methods. *Nanotechnology* **2002,** *13* (1), 33-37.

37. Nelson, B. A.; King, W. P., Temperature calibration of heated silicon atomic force microscope cantilevers. *Sensor Actuat. a-Phys.* **2007,** *140* (1), 51-59.

38. Neumeister, J. M.; Ducker, W. A., Lateral, normal, and longitudinal spring constants of atomic-force microscopy cantilevers. *Rev. Sci. Instrum* **1994,** *65* (8), 2527-2531.

39. Socoliuc, A.; Bennewitz, R.; Gnecco, E.; Meyer, E., Transition from stick-slip to continuous sliding in atomic friction: Entering a new regime of ultralow friction. *Phys. Rev. Lett.* **2004,** *92* (13).

40. Szoszkiewicz, R., Comment on *Print your atomic force microscope*. *Rev. Sci. Instrum.* **2007,** *78* (3), 037105.

41. Chen, C. J., Atomic Force Microscopy. In *Introduction to Scanning Tunneling Microscopy*, Brook, R. J., Ed. Oxford University Press: Oxford, 2008; pp 349-369.

42. Vettiger, P.; Despont, M.; Drechsler, U.; Durig, U.; Haberle, W.; Lutwyche, M. I.; Rothuizen, H. E.; Stutz, R.; Widmer, R.; Binnig, G. K., The Millipede – More than one thousand tips for future AFM data storage. *IBM J. Res. Dev.* **2000,** *44* (3), 323-340.

43. Fenwick, O.; Bozec, L.; Credgington, D.; Hammiche, A.; Lazzerini, G. M.; Silberberg, Y. R.; Cacialli, F., Thermochemical nanopatterning of organic semiconductors. *Nat. Nanotechnol* **2009,** *4* (10), 664-668.

44. Wang, D. B.; Szoszkiewicz, R.; Lucas, M.; Riedo, E.; Okada, T.; Jones, S. C.; Marder, S. R.; Lee, J.; King, W. P., Local wettability modification by thermochemical nanolithography with write-read-overwrite capability. *Appl. Phys. Lett.* **2007,** *91* (24).

45. Haydell, M.; Cimpoiaus, E.; Lee, W.; Sheehan, P. E.; Stine, R. R.; King, W. P., Direction writing of graphene-based nanoribbons via thermochemical nanolithography. In *Microsystems for Measurement and Instrumentation*, Firebaugh, S., Ed. United States Naval Academy, 2012; pp 1 – 3

46. Lee, J.; Beechem, T.; Wright, T. L.; Nelson, B. A.; Graham, S.; King, W. P., Electrical, thermal, and mechanical characterization of silicon microcantilever heaters. *J. Microelectromech S.* **2006,** *15* (6), 1644-1655.

47. Fryer, D. S.; Nealey, P. F.; de Pablo, J. J., Thermal probe measurements of the glass transition temperature for ultrathin polymer films as a function of thickness. *Macromolecules* **2000,** *33* (17), 6439-6447.

48. Fryer, D. S.; Peters, R. D.; Kim, E. J.; Tomaszewski, J. E.; de Pablo, J. J.; Nealey, P. F.; White, C. C.; Wu, W. L., Dependence of the glass transition temperature of polymer films on interfacial energy and thickness. *Macromolecules* **2001,** *34* (16), 5627-5634.

49. Raab, M.; Nezbedova, E., Toughness of Ductile Polymers. In *Performance of Plastics*, Brostow, W., Ed. Hanser: Munich – Cincinnati, 2000; pp 46-62.

50. Chui, B. W.; Asheghi, M.; Ju, Y. S.; Goodson, K. E.; Kenny, T. W.; Mamin, H. J., Intrinsic-carrier thermal runaway in silicon microcantilevers. *Microscale Therm. Eng.* **1999,** *3* (3), 217-228.

51. Hall, D. B.; Underhill, P.; Torkelson, J. M., Spin coating of thin and ultrathin polymer films. *Polym. Eng. Sci.* **1998,** *38* (12), 2039-2045.

52. Bornside, D. E.; Macosko, C. W.; Scriven, L. E., Spin Coating – One-Dimensional Model. *J. Appl. Phys.* **1989,** *66* (11), 5185-5193.

53. Bornside, D. E.; Macosko, C. W.; Scriven, L. E., On the Modeling of Spin Coating. *J. Imaging Technol.* **1987,** *13* (4), 122-130.

54. Schubert, D. W.; Dunkel, T., Spin coating from a molecular point of view: its concentration regimes, influence of molar mass and distribution. *Mater. Res. Innov.* **2003,** *7* (5), 314-321.

55. Kim, S. H.; Misner, M. J.; Xu, T.; Kimura, M.; Russell, T. P., Highly oriented and ordered arrays from block copolymers via solvent evaporation. *Advanced Materials* **2004,** *16* (3), 226-229.

56. Mokarian-Tabari, P.; Collins, T. W.; Holmes, J. D.; Morris, M. A., Brushless and Controlled Microphase Separation of Lamellar Polystyrene-b-Polyethylene Oxide Thin Films for Block Copolymer Nanolithography. *Journal of Polymer Science Part B-Polymer Physics* **2012,** *50*, 904-909.

57. Nelson, B. A.; King, W. P., Modeling and simulation of the interface temperature between a heated silicon tip and a substrate. *Nanoscale and Microscale Thermophysical Engineering* **2008,** *12* (1), 98-115.

58. Nelson, B. A.; King, W. P., Measuring material softening with nanoscale spatial resolution using heated silicon probes. *Rev. Sci. Instrum.* **2007,** *78* (2).

59. Duvigneau, J.; Schonherr, H.; Vancso, G. J., Nanoscale Thermal AFM of Polymers: Transient Heat Flow Effects. *ACS Nano* **2010,** *4* (11), 6932-6940.

60. Maugis, D., *Contact, Adhesion and Rupture of Elastic Solids*. Springer-Verlag: Berlin, 1999.

61. Yoshizawa, H.; Israelachvili, J., Fundamental Mechanisms of Interfacial Friction .2. Stick-Slip Friction of Spherical and Chain Molecules. *Journal of Physical Chemistry* **1993,** *97* (43), 11300-11313.

62. Noteworthy, we did not observe any lamellar phases in the case of PS-b-PEO films being solely spin cast on Si substrate and annealed thermally. .

63. Schmidt, R. H.; Haugstad, G.; Gladfelter, W. L., Scan-induced patterning in glassy polymer films: Using scanning force microscopy to study plastic deformation at the nanometer length scale. *Langmuir* **2003,** *19* (3), 898-909.

64. Aoike, T.; Yamamoto, T.; Uehara, H.; Yamanobe, T.; Komoto, T., Surface deformation properties of polystyrene as evaluated from the morphology of surfaces scratched by using the tip of a scanning force microscope. *Langmuir* **2001,** *17* (18), 5688-5692.

65. Meyers, G. F.; Dekoven, B. M.; Seitz, J. T., Is the Molecular Surface of Polystyrene Really Glassy? *Langmuir* **1992,** *8* (9), 2330-2335.

66. Whitmore, M. D.; Noolandi, J., Theory of Crystallizable Block Copolymer Blends. *Macromolecules* **1988,** *21* (5), 1482-1496.

67. Dimarzio, E. A.; Guttman, C. M.; Hoffman, J. D., Calculation of Lamellar Thickness in a Diblock Co-Polymer, One of Whose Components Is Crystalline. *Macromolecules* **1980,** *13* (5), 1194-1198.

68. Helfand, E.; Wasserman, Z. R., Block Copolymer Theory .5. Spherical Domains. *Macromolecules* **1978,** *11* (5), 960-966.

69. Unger, R.; Beyer, D.; Donth, E., Phase-Behavior in Poly(Ethylene Oxide-B-Tert-Butyl Methacrylate) Block Copolymers. *Polymer* **1991,** *32* (18), 3305-3312.

70. Lee, L. B. W.; Register, R. A., Equilibrium control of crystal thickness and melting point through block copolymerization. *Macromolecules* **2004,** *37* (19), 7278-7284.

71. Hashimoto, T.; Fujimura, M.; Kawai, H., Domain-Boundary Structure of Styrene-Isoprene Block Co-Polymer Films Cast from Solutions .5. Molecular-Weight Dependence of Spherical Microdomains. *Macromolecules* **1980,** *13* (6), 1660-1669.

72. For example 50 % error in E_{fold} yields 16 % uncertainty in d_{EQ}.

73. Takahash.Y; Tadokoro, H., Structural Studies of Polyethers, (-(Ch2)M-O-)N .10. Crystal-Structure of Poly(Ethylene Oxide). *Macromolecules* **1973,** *6* (5), 672-675.

74. We neglect any tilt angle of the PEO chains here.

75. Jeng, U. S.; Sun, Y. S.; Lee, H. Y.; Hsu, C. H.; Liang, K. S.; Yeh, S. W.; Wei, K. H., Binding effect of surface-modified cadmium sulfide on the microstructure of PS-b-PEO block copolymers. *Macromolecules* **2004,** *37* (12), 4617-4622.

76. Lin, Z. Q.; Kim, D. H.; Wu, X. D.; Boosahda, L.; Stone, D.; LaRose, L.; Russell, T. P., A rapid route to arrays of nanostructures in thin films. *Advanced Materials* **2002,** *14* (19), 1373-1376.

77. Kim, J. K.; Han, C. D., Phase Behavior and Phase Transitions in AB- and ABA-type Microphase-Separated Block Copolymers. In *Polymer Materials: Block-Copolymers, Nanocomposites, Organic/Inorganic Hybrids, Polymethylenes*, Lee, K. S.; Kobayashi, S., Eds. 2010; Vol. 231, pp 77-145.

78. Matsushita, Y.; Noda, I.; Nagasawa, M.; Lodge, T. P.; Amis, E. J.; Han, C. C., Expansion factor of a part of a polymer chain in a good solvent measured by small-angle neutron scattering. *Macromolecules* **1984,** *17* (9), 1785-1789.

79. Tata, J.; Scalarone, D.; Lazzari, M.; Chiantore, O., Control of morphology orientation in thin films of PS-b-PEO diblock copolymers and PS-b-PEO/resorcinol molecular complexes. *European Polymer Journal* **2009,** *45* (9), 2520-2528.

80. Mokarian-Tabari, P.; Collins, T. W.; Holmes, J. D.; Morris, M. A., Cyclical Flipping of Morphology in Block Copolymer Thin Films. *ACS Nano* **2011,** *5* (6), 4617-4623.

81. Flanders, B. N., Directed Electrochemical Nanowire Assembly: Precise Nanostructure Assembly via Dendritic Solidification. *Modern Physics Letters B* **2012,** *26* (1), 1130001-1 - 1130001-33.

82. Kessler, D. A.; Koplik, J.; Levine, H., Pattern Selection in Fingered Growth Phenomena. *Advances in Physics* **1988,** *37* (3), 255-339.

83. Zhai, X. M.; Wang, W.; Ma, Z. P.; Wen, X. J.; Yuan, F.; Tang, X. F.; He, B. L., Spontaneous and inductive thickenings of lamellar crystal monolayers of low molecular weight PEO fractions on surface of solid substrates. *Macromolecules* **2005,** *38* (5), 1717-1722.

84. Zhai, X. M.; Wang, W.; Zhang, G. L.; He, B. L., Crystal pattern formation and transitions of PEO monolayers on solid substrates from nonequilibrium to near equilibrium. *Macromolecules* **2006,** *39* (1), 324-329.

85. Woodland, D. D.; Unertl, W. N., Initial wear in nanometer-scale contacts on polystyrene. *Wear* **1997,** *203*, 685-691.

86. Elkaakour, Z.; Aime, J. P.; Bouhacina, T.; Odin, C.; Masuda, T., Bundle Formation of Polymers with an Atomic-Force Microscope in Contact Mode – a Friction versus Peeling Process *Phys. Rev. Lett.* **1994,** *73* (24), 3231-3234.

87. Nishimori, H.; Ouchi, N., Formation of Ripple Patterns and Dunes by Wind-Blown Sand. *Phys. Rev. Lett.* **1993,** *71* (1), 197-200.

88. The value of *R* was obtained from tip-sample deconvolution in Figure 2.2C.

89. We used SiNx Young modulus of 304 Gpa, its Poisson ratio of 0.24, thickness of a cantilever of 0.60 ± 0.05 μm, triangle opening angle of 28 ± 2 degr, the length of cantilever's arms from the base towards the point they meet of 195 ± 10 μm, the distance from the tip to the edge of a cantilever 5 ± 1 μm, the cantilever's arm width of 18 ± 1 μm, and the tip's height of 7 ± 1 μm.

90. These were obtained from FWHH at visible indents in Figure 2.2C. Some of these indents were marked as black circles in Figure 2.2C.

91. Schmidt, R. H.; Haugstad, G.; Gladfelter, W. L., Correlation of nanowear patterns to viscoelastic response in a thin polystyrene melt. *Langmuir* **1999,** *15* (2), 317-321.

92. Sills, S.; Overney, R. M.; Chau, W.; Lee, V. Y.; Miller, R. D.; Frommer, J., Interfacial glass transition profiles in ultrathin, spin cast polymer films. *Journal of Chemical Physics* **2004,** *120* (11), 5334-5338.

93. Bliznyuk, V. N.; Assender, H. E.; Briggs, G. A. D., Surface glass transition temperature of amorphous polymers. A new insight with SFM. *Macromolecules* **2002,** *35* (17), 6613-6622.

94. Schonherr, H.; Frank, C. W., Ultrathin films of poly(ethylene oxides) on oxidized silicon. 2. In situ study of crystallization and melting by hot stage AFM. *Macromolecules* **2003,** *36* (4), 1199-1208.

95. Pfefferkorn, D.; Kyerematen, S. O.; Busse, K.; Kammer, H.-W.; Thurn-Albrecht, T.; Kressler, J., Crystallization and Melting of Poly(ethylene oxide) in Blends and Diblock Copolymers with Poly(methyl acrylate). *Macromolecules* **2011,** *44* (8), 2953-2963.

96. Fakhraai, Z.; Forrest, J. A., Probing slow dynamics in supported thin polymer films. *Phys Rev Lett* **2005,** *95* (2).

97. Williams, M. L.; Landel, R. F.; Ferry, J. D., Mechanical Properties of Substances of High Molecular Weight .19. The Temperature Dependence of Relaxation Mechanisms in Amorphous Polymers and Other Glass-Forming Liquids. *Journal of the American Chemical Society* **1955,** *77* (14), 3701-3707.

98. Ferry, J. D., *Viscoelastic Properties of Polymers*. Wiley & Sons: New York, 1980.

99. We used indentation of about 5 nm and tip curvature radius of ~ 40 nm.

100. Due to three orders of magnitude higher thermal conductivity of silicon as compared to polymers.

101. In particular, our surface temperature is about three times smaller than 250 ^{o}C used in Fenwick, et al., Nature Nanotech 4, 664 (2009), but their 70 ^{o}C isotherm is exactly three times wider then their initial lateral probe contact width, which lets us read the critical core width value from their Figure 4b for 30 nm contact width and 8 nm (instead of 30 nm) thickness of the polymer film.

102. Such, B.; Krok, F.; Szymonski, M., AFM tip-induced ripple pattern on AIII-BV semiconductor surfaces. *Appl. Surf. Sci.* **2008,** *254* (17), 5431-5434.

103. Mulhearn, T. O.; Samuels, L. E., The Abrasion of Metals: A Model of the Process. *Wear* **1963,** *5* (6), 478-498.

104. Schmidt, R. H.; Haugstad, G.; Gladfelter, W. L., Scan-induced patterning and the glass transition in polymer films: Temperature and rate dependence of plastic deformation at the nanometer length scale. *Langmuir* **2003,** *19* (24), 10390-10398.

105. Steiner, P.; Roth, R.; Gnecco, E.; Baratoff, A.; Maier, S.; Glatzel, T.; Meyer, E., Two-dimensional simulation of superlubricity on NaCl and highly oriented pyrolytic graphite. *Phys. Rev. B* **2009,** *79* (4).

106. Plazek, D.; Ngai, K., The Glass Temperature. In *Physical Properties of Polymers Handbook*, 2nd ed.; Ma r k, J. E., Ed. Spinger Science Cincinnati, 2007.

Appendix A. WaveMetrics, Inc. IGOR Pro software coding

This appendix provides specific coding used in the IGOR Pro software. Section A.1 is used to move the AFM scanner in an Archimedes spiral and section A.2 is coding used to process data. A.2 is provided for anyone wanting to have a way to find peaks and troughs within an IGOR wave. Note that all comments that are not directly related to coding are of the following format: //{comment}, these will help anyone wanting to change the coding to suit their needs. Also, be sure to check the coding line for line as copying and pasting between IGOR and word will cause some characters to change.

A.1. Spirals

In order to generate the spiral pattern of the scanner used in Chapter 3, hardware methods discussed in Chapter 1.3. gave control of the scanner to the IGOR computer. The procedure below is the coding used to generate the Archimedes spiral pattern sent to the scanner. The code was written by Dr. R. Szoszkiewicz and is published here with his permission, but for non-commercial use only.

```
#pragma rtGlobals=1                                    // Use modern global access method.

//////////////////////////////////////////////
// Activate via RipplesSetupPanel()
//
//////////////////////////////////////////////

Menu "Macros"
        "-"
        "Ripples Controls", RipplesSetupPanel()
        "ZeroXYSignals", ZeroXYSignals()
        "-"
End

Override Function Initial_Values()                     // Initialization
        NewDataFolder/O root:Variables
        NewDataFolder/O root:Config

        Variable /G root:Variables:CircleRadius        = 6000   //nm
        Variable /G root:Variables:CircleFreq          = 0.5    //Hz
        Variable /G root:Variables:NumCycles           = 20     //s
        Variable /G root:Variables:ExperTime

        Variable /G root:Variables:TipTemperature      = 250    //deg C
        Variable /G root:Variables:Temperature         = 27     //deg C
```

```
Variable /G  root:Variables:Humidity                = 45      // %
Variable /G root:Variables:AFMTipVelocity

Variable /G root:Variables:XpiezoScale              = 4000    //nm/V   As done by Anthony
Variable /G root:Variables:YpiezoScale              = 4000    //nm/V   CHECK IT !!!!!!!!!!

Variable /G root:Variables:NyquistFraction          = 1             //for filtering the signal
Variable /G root:Variables:SamplingFrequency        = 2E4     //inverse of  the dt spacing between
                                                              sent/acquired data points
Variable /G root:Variables:DeltaT                             // inverse of sampling frequency
Variable /G root:Variables:FilterFrequency                    //half the sampling freq. due to Nyquist
                                                              theorem

Variable /G root:Variables:AplusBGain               =1        //defines the sensitivity of data acquisition,
                                                              i.e., +/-10/gain is the voltage range of data
                                                              acquisition
Variable /G root:Variables:AminusBGain              =1
Variable /G root:Variables:LFMGain                  =1

Variable/G root:Variables:WriteFileNumber           =1
Variable/G root:Variables:XcommandRange
Variable/G root:Variables:YcommandRange


SetFormula root:Variables:AFMTipVelocity,"2*Pi*root:Variables:CircleRadius*root:Variables:CircleFreq"
SetFormula root:Variables:ExperTime ,       "root:Variables:NumCycles/root:Variables:CircleFreq"
SetFormula root:Variables:FilterFrequency,  "root:Variables:SamplingFrequency /2"
SetFormula root:Variables:DeltaT,  "1/root:Variables:SamplingFrequency"

                                                              // prepares the DAQ
fDAQmx_ResetDevice("Dev1")
SetDataFolder root:Config

                                                              // Prepare information about last self-
                                                              calibration of DAQs
String/G root:Config:LastSelfCalibrationDev1 = "PCI-6289 (Dev1) last self-calibration: "
SVAR LastSelfCalibrationDev1 = root:Config:LastSelfCalibrationDev1

Variable TimeNow = DateTime                                   //The time now, as we run the
                                                              procedure, in Igor format (seconds since
                                                              1/1/1904)
Variable Dev1SCT = fDAQmx_SelfCalDate("Dev1")                 //Time since last self-calibration of
                                                              Device 1
Variable MaxUncalibrateTime = (60*60*24)*7                    //(sec * min* hours)* days <= how many
                                                              days between self-calibrate

If(numtype(Dev1SCT) ==0)
        If(TimeNow-Dev1SCT>MaxUncalibrateTime)
                LastSelfCalibrationDev1   += "\\K(65280,0,0)"
                Print "You should self-calibrate Dev1 -> close Igor, go to Meas&Instrum Program, then
                return to Igor"
        Else
                LastSelfCalibrationDev1   += "\\K(0,52224,0)"
                Print "No need to self-calibrate Dev1 today -> continue working with Igor"
        EndIF
        LastSelfCalibrationDev1 +=Secs2Date(Dev1SCT, 2 )
Else
        LastSelfCalibrationDev1 += "\\K(0,9472,39168) Unknown"
```

```
	EndIF

	String SaveHistory="History of saved traces"
	DoWindow NotebookSaveHistory
	if(V_Flag==1)
		DoWindow/F/D NotebookSaveHistory
	else
		NewNotebook/K=0/f=0/N=NotebookSaveHistory/W=(600,0,800,120) as SaveHistory
	endif

End
////////////////////////////////////////////////////////////////////////
Window RipplesSetupPanel() : Panel
	PauseUpdate; Silent 1                                    // building window...
	Initial_Values()
	NewPanel /W=(525,492,1062,782) as "Nanoscale Ripples Data Acquisition Panel"
	//ShowTools

	Button RipplesStart,pos={60, 230},size={63,41},proc=StartRipples,title="Start"
	Button RipplesStart,fColor=(52224,0,0)
	Button RipplesStop,pos={160, 230},size={93,41},proc=StopRipples,title="STOP \r click abort first"
	Button RipplesStop,fColor=(0,0,65280)
	SetVariable VarCircleRadius,pos={30,43},size={220,16},title="Circle radius (nm)"
	SetVariable VarCircleRadius,limits={0,50000,5},value= root:Variables:CircleRadius,bodyWidth= 60
	SetVariable VarCircleFreq,pos={30,69},size={220,16},title="Circle frequency (Hz)"
	SetVariable VarCircleFreq,limits={0.05,100,0.05},value= root:Variables:CircleFreq,bodyWidth= 60
	ValDisplay VarTipVelocity,pos={30,95},size={220,16},title="approx. AFM tip velocity
                                                              nm/s",limits={0,0,0}
	ValDisplay VarTipVelocity,format="%1.2e"
	ValDisplay VarTipVelocity,value= #"root:Variables:AFMTipVelocity"
	SetVariable VarNumCycles,pos={20,121},size={120,16},title="# cycles?"
	SetVariable VarNumCycles,limits={1,1000,1},value= root:Variables:NumCycles,bodyWidth= 60
	ValDisplay VarExpTime,pos={145,121},size={130,10},title="Exper. Time (s)",limits={0,0,0}
	ValDisplay VarExpTime,format="%.1f"
	ValDisplay VarExpTime,value= #"root:Variables:ExperTime"
	SetVariable VarSamplingFreq,pos={30,147},size={230,16},title="Data sampling freq. (Hz)"
	SetVariable VarSamplingFreq,limits={1E3,1E5,1E2},value= root:Variables:SamplingFrequency
	SetVariable VarSamplingFreq,format="%1.1e", bodyWidth=70
	ValDisplay VarSamplingTime,pos={30,173},size={230,16},title="dt between data points (s)"
	ValDisplay VarSamplingTime,value= #"root:Variables:DeltaT"
	ValDisplay VarSamplingTime,format="%1.1e", bodyWidth=60
	ValDisplay VarNpoints,pos={30,199},size={220,16},title="# points in the cycle",bodyWidth= 60
	ValDisplay VarNpoints,value= #"floor(root:Variables:SamplingFrequency/root:Variables:CircleFreq)"

	SetVariable ExtrasXCalibFactor,pos={340,43},size={150,16},title="X piezo scale (nm/V)"
	SetVariable ExtrasXCalibFactor,limits={10,15000,1},value= root:Variables:XpiezoScale,bodyWidth= 60
	SetVariable ExtrasYCalibFactor,pos={340,69},size={150,16},title="Y piezo scale (nm/V)"
	SetVariable ExtrasYCalibFactor,limits={10,15000,1},value= root:Variables:YpiezoScale,bodyWidth= 60
	SetVariable ExtrasTipTemperature,pos={340,121},size={150,16},title="AFM tip temp. "I"
	SetVariable ExtrasTipTemperature,limits={0,600,5},value= root:Variables:TipTemperature,bodyWidth=
                                                              60
	SetVariable ExtrasTemperature,pos={340,147},size={150,16},tit"e="Air temperatu"I(C)"
	SetVariable ExtrasTemperature,limits={0,50,1},value= root:Variables:Temperature,bodyWidth= 60
	SetVariable ExtrasHumidity,pos={340,173},size={150,16},"itle="Air rel. humidi"y (%)"
	SetVariable ExtrasHumidity,limits={0,100,1},value= root:Variables:Humidity,bodyWidth= 60
	SetVariable ExtrasNyFraction,pos={340,225},size={150,16},"itle="Nyquist Fr"ction"
	SetVariable ExtrasNyFraction,limits={0,1,0.01},value= root:Variables:NyquistFraction,bodyWidth= 60
```

```
	GroupBox Var,pos={20,13},size={260,268},”itle="Initial Var”ables"
	GroupBox Extras,pos={300,13},size={205,268},”itle="”xtras"
EndMacro

////////////////////////////////////////////////////////////////////////////
Function CreateCommand(name,amplitude,offset, phase, numPoints)    //Creates ramp of piezo
	String name
	Variable amplitude, offset, phase, numPoints

	NVAR freq = root:Variables:CircleFreq
	NVAR duration = root:Variables:ExperTime

	Make/O/N=(numPoints) $name
	Wave w=$name
                                                                    // t=total duration *p/number of points
	w = amplitude*(p/numPoints)*Sin(((Pi)/180)*(360*(p/numPoints)*freq*duration  + phase) )
	w=w+offset
End

////////////////////////////////////////////////////////////////////////////
Function ZeroXYSignals()                                            //zeros X and Y channels after doing the
                                                                    spiral, keeps the same card range as for the
                                                                    signal acquisition
	NVAR XCommandRange=root:Variables:XCommandRange
	NVAR YCommandRange=root:Variables:YCommandRange

fDAQmx_Writ“Chan”"Dev1", 0, 0, -XCommandRange,XCommandRange)
fDAQmx_Writ“Chan”"Dev1", 1, 0, -YCommandRange,YCommandRange)

End

Function StartRipples(ctrlName) : ButtonControl
	String ctrlName

	NVAR NumCyc = root:Variables:NumCycles
	NVAR TotDuration = root:Variables:ExperTime
	NVAR Size = root:Variables:CircleRadius                         // in nm
	nVAR XScale = root:Variables:XPiezoScale                        // in nm/V
	nVAR YScale = root:Variables:YPiezoScale
	NVAR NyquistFraction = root:Variables:NyquistFraction
	NVAR FilterFrequency = root:Variables:FilterFrequency
	NVAR SamplingFrequency = root:Variables:SamplingFrequency
	NVAR DeltaT = root:Variables:DeltaT
	NVAR AplusBGain = root:Variables:AplusBGain
	NVAR AminusBGain = root:Variables:AminusBGain
	NVAR LFMGain = root:Variables:LFMGain
	nVAR XCommandRange=root:Variables:XCommandRange
	nVAR YCommandRange=root:Variables:YCommandRange

	Variable XAmplitude, YAmplitude, Offset, Npnts, NpntsCommand    //, XCommandRange,
                                                                    YCommandRange
	Variable Backg
	String DA_String, AD_String                                     // to stop any background
                                                                    scanning processes at the beginning
	BackgroundInfo
	Backg = V_Flag
```

```
if (Backg==2)
        CtrlBackground stop
endif

                                                        // define waves and set frequencies
                                                        to match PCI-6289 capabilities!
XAmplitude = (size/XScale)                              //in V to be sent to the
                                                        microscope
YAmplitude = (size/YScale)                              //in V to be sent to the microscope

                                                        //time spacing between
                                                        consecuitive data points -> NOW
                                                        global variable
                                                        //DeltaT = (1/SamplingFrequency)
                                                        //minimal delta time between data
                                                        points, i.e., 1/sampling frequency,
                                                        // for OUTput channels 2.8
                                                        MSamples/s, but for input only 500
                                                        kSamples/s (multichannels) (NI
                                                        PCI 6289)
                                                        // so to match input and output
                                                        waves, 500 kSamples/s is max for
                                                        both.
                                                        // 5 kHz used just for now !!!!!!!!
                                                        There were Problems with 500
                                                        kHz, but 5kHz is enough


Npnts =   floor(TotDuration/DeltaT)                     // Npoints for command wave
                                                        depends on the type of data
                                                        acquisition process
NpntsCommand = 3*Npnts                                  // WE SUPpOSE! that we trigger
data acquisition by input waves! Than there is three input waves (A+B, A-B, LFM)  and each point of each of these
input waves is scanned clock“d by "”eltaT", so Output waves (fast speed of 2.8MS/s), need to have (number of input
channels = 3) “imes "data ”oints" separated by DeltaT, and INPUT waves will“have "data ”oints" separated by 3x
time spacing otherwise: t1=t_start: output channels send and one input wave scanned, t2=t1+deltaT: output channels
sent and another input  wave scanned, t3=t1+2*DeltaT: output channel sent, and third input wave scanned, t4: as
t_start;
Offset = 0

CreateCommand("XCommand", XAmplitude,Offset, 90, NpntsCommand)
                                                        //Create X sin wave // cos from 12/6/2011
CreateCommand("YCommand", YAmplitude,Offset, 0, NpntsCommand)
                                                        //Create Y cosine wave //sin from 12/6/2011

Make/O/N=(Npnts) AplusB = NaN, AminusB = NaN, LFM = NaN      //create receiving waves with one
                                                        third of the # of command points/channel for
                                                        three channels
SetScale/I x 0,TotDura“i”n, "s", XCommand, YCommand, AplusB, AminusB, LFM
                                                        //set acquisition rate by scaling th“m to
                                                        "TotDuration”, get data as fast as possible,
                                                        but later filter!!!


                                                        // use IGOR filters!!!!
FilterFrequency =  (1/DeltaT)/2 * NyquistFraction       //NyquistFreq * NyquistFraction =
                                                        Sampling Freq/2 * NyFraction
```

```
	sleep/s 0.5

	                                                    //execute simultaneous A/D and D/A, and
	                                                    redefine X, Y command ranges
	XCommandRange = min(10, XAmplitude)
	YCommandRange = min(10, YAmplitude)
	DA_String = "XCommand, 0,"+Num2str(-XCommandRange)+","+Num2Str(XCommandRange)+";
YCommand,1,"+Num2str(-YCommandRange)+","+Num2Str(YCommandRange)+";"
	AD_String = "AplusB,0”Diff,"+Num2Str(-
10/AplusBGain)+","+Num2Str(10/AplusBGain)+";AminusB,1/Diff,"+Num2Str(-
10/AminusBGain)+","+Num2Str(10/AminusBGain)+";LFM,2/Diff,"+Num2Str(-
10/LFMGain)+","+Num2Str(10/LFMGain)+";"


	                                                    // the way we do spiral leaves max.
	                                                    voltage on Y channel from a previous spiral,
	                                                    we have to zero the initial voltage

	DAQmx_WaveformGen/“RIG={"/dev1/ai/starttrigger"}/DEV”"Dev1"/NPRD=1 DA_String
	DAQmx_Scan/BKG/DEV=”Dev1" WAVES=AD_String

	DoWindow OscilloscopeDisplay
	if (V_Flag == 1)
		RemoveFromGraph/Z/W=OscilloscopeDisplay AminusB
		AppendToGraph/W=OscilloscopeDisplay AminusB
		ModifyGraph/W=OscilloscopeDisplay rgb(Force)=(0,52224,0)
	else
		DoWindow/K TemporalDisplay
		Display/K=1 AminusB
		SetAxis/A left
		DoWindow/N/C TemporalDisplay
		Label b“ttom "Ti”e (s)"
		Label“le–t "A -”B (V)"
	endif
	Do
		DoUpdate
While( !fDAQmx_ScanGetAvailable("Dev1"))                //fDAQmx_ScanGetAvai“able”"Dev1")
	                                                    returns 1 if scanning is finished so
	                                                    !fDAQmx_ScanGetAvai“able”"Dev1")
	                                                    returns 0

	fDAQmx_Wavefor“Stop”"Dev1")                         //just in case

SaveTraces()                                            //  very important
	                                                    to save the traces for future use!
End

////////////////////////////////////////////////////////////////////////////////
Function StopRipples(ctrlName) : ButtonControl
	String ctrlName

	Variable Backg
	                                                    // stop any background scanning processes at
	                                                    the beginning
	BackgroundInfo
	Backg = V_Flag
	if (Backg==2)
```

```
                CtrlBackground stop
        endif

fDAQmx_WaveformStop("Dev1")
printf "OK. No signal applied to the AFM scann”r. \r"
End

////////////////////////////////////////////////////////////////////////////////
Function SaveTraces()
        NVAR WriteFileNumber=root:Variables:WriteFileNumber
        NVAR Temperature =root:Variables:Temperature
        NVAR CircleRadius = root:Variables:CircleRadius
        NVAR CircleFreq = root:Variables:CircleFreq
        NVAR NumCycles=root:Variables:NumCycles
        NVAR ExperTime= root:Variables:ExperTime
        NVAR TipTemperature     =root:Variables:TipTemperature
        NVAR  Humidity=root:Variables:Humidity
        NVAR  AFMTipVelocity=root:Variables:AFMTipVelocity
        NvAR  XPiezoScale=root:Variables:XPiezoScale
        NvAR  YPiezoScale=      root:Variables:YPiezoScale
        NVAR  NyquistFraction=root:Variables:NyquistFraction
        NVAR  SamplingFrequency=root:Variables:SamplingFrequency
        NVAR  DeltaT=root:Variables:DeltaT
        NVAR  FilterFrequency=root:Variables:FilterFrequency
        NVAR  AplusBGain=root:Variables:AplusBGain
        NVAR  AminusBGain=root:Variables:AminusBGain
        NVAR  LFMGain           =root:Variables:LFMGain

        String AminusB_waveName, AplusB_waveName, LFM_waveName, InfoNote=""

        AminusB_waveName ="AminusB_"+Num2Str(WriteFileNumber)
        AplusB_waveName ="AplusB_"+Num2Str(WriteFileNumber)
        LFM_waveName ”"LFM_"+Num2Str(WriteFileNumber)

        Duplicate/O AminusB $AminusB_waveName
        Duplicate/O AplusB $AplusB_waveName
        Duplicate/O LFM $LFM_waveName

        InfoNote += ”Date=" + Date() + ";”Time=" + Time()
        InfoNote += "; Air temperature=" + num2str(Temperature)
        InfoNote += "; Approx. AFM temperature=" + num2str(TipTemperature)
        InfoNote += "; Relative humidity=" + num2str(Humidity)
        InfoNote += "; Circle Radius”(nm)=" + num2str(CircleRadius)
        InfoNote += "; Circle frequency”(Hz)=" + num2str(CircleFreq)
        InfoNote += "; Approx. AFM tip velocity (nm/s)=" + num2str(AFMTipVelocity)
        InfoNote +=  "; Data sampling frequency”(Hz)=" + num2str(SamplingFrequency)
        InfoNote += "; Nyquist Fraction="  + num2str(NyquistFraction)
        InfoNote += "; X piezo calib (nm of motion per V fed to its controller)=" + num2str(XPiezoScale)
        InfoNote += "; Y piezo calib (nm of motion per V fed to its controller)=" + num2str(YPiezoScale)
        Note $AminusB_waveName, InfoNote
        Note $AplusB_waveName, InfoNote
        Note $LFM_waveName, InfoNote
        Notebook NotebookSaveHistory text="Ripples recording # " + num2str(WriteFileNumber) + " saved at " +
                                        time()+ "\r"
        WriteFileNumber += 1                                            //Beep
End
```

A.2. Finding peaks and troughs of data

The IGOR procedure coding below is from John Weeks at WaveMetrics and published with his permission for non-commercial use only. WaveMetrics support can be reached at 503-620-3001. Tell the operator you want to talk to Mr. Weeks or generally explain your issue and you will be connected to the expert in that area. This procedure allows the IGOR user to find peaks and troughs of an IGOR wave and used throughout this thesis to greatly increase data processing times.

```
#pragma rtGlobals=1                                    // Use modern global access method.

                                                       // Modified 120220 by John Weeks at
                                                       WaveMetrics to use the graph cursors

Menu "Macros"
        "Find Peaks in Top GraphAB", /Q, mFindPeaksInTopGraph()
end

Function mFindPeaksInTopGraph()

        String gname = WinName(0,1)
        if (strlen(gname) == 0)
                return -1
        endif

        String tracename = StringFromList(0, TraceNameList(gname, ";", 1))
        Variable minLevel = 0
        Variable doNeg = 2
        String outbasename="OutPeaks"

        Prompt tracename, "Which graph trace contains peaks?", popup, TraceNameList(gname, ";", 1)
        Prompt minLevel, "Minimum (or maximum for negative peaks) level:"
        Prompt doNeg, "Negative peaks?", popup, "Yes;No;"
        Prompt outbasename, "Base name for output waves:"
        DoPrompt "Find Peaks in Top Graph", tracename, minLevel, doNeg, outbasename
        if (V_flag)
                return -1
        endif

        String wavenameY = GetWavesDataFolder(TraceNameToWaveRef(gname, tracename), 2)
        String wavenameX = GetWavesDataFolder(XWaveRefFromTrace(gname, tracename), 2)

                                                       // JW 120220 added test for presence of
                                                       graph cursors
        Variable startPoint, endPoint
        if (strlen(CsrInfo(A, gname)) > 0)
                startPoint = pcsr(A)
        else
                startPoint = 0
        endif
        if (strlen(CsrInfo(B, gname)) > 0)
                endPoint = pcsr(B)
        else
```

```
		endPoint = numpnts($wavenameY) - 1
	endif
	if (startPoint > endPoint)
		Variable temp = startPoint
		startPoint = endPoint
		endPoint = temp
	endif
	FindPeaksMakeXYPair($wavenameY, $wavenameX, minLevel, doNeg == 1, outbasename, startPoint,
				endPoint)

	Wave outy = $(outbasename+"Y")
	Wave outx = $(outbasename+"X")
	CheckDisplayed/W=$gname outy
	if (V_flag == 0)
		AppendToGraph/W=$gname outy vs outx
	endif
end

// JW 120220 added startPoint and endPoint inputs to support use of graph cursors.
Function FindPeaksMakeXYPair(inY, inX, minLevel, doNeg, outbasename, startPoint, endPoint)
	Wave inY, inX
	Variable minLevel		// Peaks below (or above for doNeg true) this level are not peaks
	Variable doNeg			// find the minima instead of the maxima'
	String outbasename
	Variable startPoint, endPoint

	// JW 120220 changed initialization of startP and endP to support use of graph cursors.
	Variable startP = startPoint
	Variable endP = endPoint
	Make/N=(numpnts(inY))/O/D $(outbasename+"Y"), $(outbasename+"X")	//
Make/N=(numpnts(inY))/O/D $(outbasename+"Y") /WAVE=outPeaksY, $(outbasename+"X")/WAVE=outPeaksX
	WAVE outPeaksY=$(outbasename+"Y")
	Wave outPeaksX=$(outbasename+"X")
	outPeaksY = NaN
	outPeaksX = NaN
	Variable peakNumber = 0
	Variable peakPoint
	Do
		if (doNeg)
			FindPeak/M=(minLevel)/N/P/I/Q/R=(startP, endP)/B=0 inY
			if (V_flag)
				break;
			endif
			peakPoint = inY[floor(V_peakLoc)] < inY[ceil(V_peakLoc)] ? floor(V_peakLoc) :
								ceil(V_peakLoc)
		else
			FindPeak/M=(minLevel)/P/I/Q/R=(startP, endP)/B=0 inY
			if (V_flag)
				break;
			endif
			peakPoint = inY[floor(V_peakLoc)] > inY[ceil(V_peakLoc)] ? floor(V_peakLoc) :
ceil(V_peakLoc)
		endif
		outPeaksY[peakNumber] = inY[peakPoint]
```

```
            outPeaksX[peakNumber] = inX[peakPoint]
            peakNumber += 1
            startP = ceil(V_PeakLoc)
        while(1)

        Redimension/N=(peakNumber) outPeaksY, outPeaksX                    // remove extra points
end
```

Appendix B. Calculations of the equilibrium lamellar spacing, dEQ, using the model of Whitmore and Noolandi

The equilibrium value of d_{EQ} comes from the minimization (with respect to distance d) of the free energy of the amorphous and crystalline parts as described in the Equation 7.4 in the paper of Whitmore and Noolandi.[66]

The code in Mathematica 6.0, Wolfram Research, USA (pasted below) reproduces the calculations of the model in the case of the copolymer in Chapter 2. There are several parameters in the model, which originate in Eq. 7.1 in Whitmore and Noolandi,[66] and are labeled and discussed briefly below.

ClearAll["Global`*"]	This command clears all previous variables stored in the memory
fB[d_]:=((rhoOC)/(rhoOA))*(1/Zc) *(W*c*rhoOB*Zc/(R*rhoOC*d)-1)*(EkbT)	This is the free energy of the crystalline part, see Eq. 7.1 in Whitmore and Noolandi, explanation of the key parameters below
PhiCA = Zca*rhoOC/(Zc*rhoOA) $Assumptions=Zca>0	Prepare to define the free energy of the amorphous part
alpha[d_]:= ((3/Zca)^(1/2))*(PhiCA*d)/ba	Universal function "α" in the Whitmore and Noolandi paper
gammaA = ((Zca)^(-1/2))	Universal function "γ" in the Whitmore and Noolandi paper
gAred[d_]:=0.016*alpha[d]^(muA)/((gammaA)^(1/2)) +0.74/(alpha[d]*gammaA)+0.21	Free energy function of "γ" and "α" for the amorphous, PS, part
fA[d_]:= PhiCA*gAred[d]/Zca	This is a complete free energy of the amorphous part, see Eq. 7.1 in Whitmore and Noolandi
	We enter numerical values for the parameters next
muA = 2.5	This is an arbitrary parameter in the model, discussion in Whitmore and Noolandi, p. 1489
ba =0.68	Kuhn's length of the PS, references in the main text
EkbT = 16/4.1	Interaction energy (or energy gain), E, per each fold in a single PEO molecule, the value of E=16 pN*nm is cited after Whitmore and Noolandi, and provided in the units of kB*T, which is 4.1 pN*nm at room temperature; EkbT is the most contentious parameter in our estimation, and we use 50% of error of its determination to estimate the error of dEQ
W =1	Number of layers in a given lamella
R =7	Crystallographic parameter for the PEO to say that PEO crystallizes in 7-2 helix (R=7), with a pitch "c"
c=1.95	Crystallographic parameter for the PEO, see

	above
Zca = 130	Degree of the polymerization for PS
Zcb = 350	Degree of the polymerization for PEO
Zc = Zca + Zcb	
Mca=104.15*Zca	Molar mass of the PS
Mcb = 44*Zcb	Molar mass of the PEO
t=20	Temperature in degrees of Celsius
rhoOA=5.782/(0.9199+5.098*(10^(-4))*t+2.354*(10^(-7))*t+(32.46+0.1017*t)/Mca)	Formula for the density of the PS, references in Whitmore and Noolandi
rhoOB = 16.9	Density of the PEO, units of densities are here in nm^{-3}
rhoOC=(rhoOA*rhoOB)*(Zca+Zcb)/(Zca *rhoOB+Zcb*rhoOA)	Weighted density of the PS-b-PEO
Now we solve the main equation, i.e. then minimization equation for dEQ= fA + fB with respect to a distance "d"	
Solve[D[fA[d],d]+D[fB[d],d]==0, d] {{d→-12.8663-56.3711i},{d→- 12.8663+56.3711i},{d→57.8208}} d/.Solve[D[fA[d],d]+D[fB[d],d]==0, d][[3]] 57.8208	We use only the real solution of this equation
dPS=(d/.Solve[D[fA[d],d]+D[fB[d],d]==0, d][[3]])*Zca/Zc dPEO=(d/.Solve[D[fA[d],d]+D[fB[d],d]==0, d][[3]])*Zcb/Zc **15.6598** **42.161**	The corresponding thicknesses of the PS and the PEO parts are calculated

Appendix C. Details of thermal tip calibration steps

Step 1. The local heating of the film was done with a resistively heated probe (rh lever) attached to a home-made cartridge. To obtain the tip temperature, the probe is in series with a resistor of a known resistance (1985 ± 3 ohms) and a commercial voltage generator, model E3620A, from Agilent, USA. To find the tip temperature one relates the temperature of the tip to the applied generator voltage. The temperature of the cantilever tip cannot be easily measured directly, but known is that tip temperature is linearly related to the power delivered to the cantilever.[46] Thus, one measures the voltage across the known resistor with a voltmeter.

Let "V_e" be the voltage across the known resistor, "V_s" be the generator voltage, "V_c" be the voltage across the cantilever, "R_e" be the known resistor value, "R_c" be the cantilever resistance, "I" be the current in the circuit, "P_c" be the power delivered to the cantilever, "T" be the temperature of the tip, "a" be the slope of the temperature-power graph, and "B" be the room temperature in Celsius.

With these relations:

$$V_c = V_s - V_e$$
$$I = V_e/R_e$$
$$R_c = V_c/I$$
$$P_c = V_c*I$$
$$T = a*P_c + B$$

and thus,

$$T = a*(V_s-V_e)*V_e/R_e + B$$

All these quantities are measurable except "a". To find "a", use the fact that at approximately 550^o C, the cantilever begins thermal runway and its resistance starts to drop rapidly.[46] One can find the power that corresponds to this event by measuring the external voltage for various generator voltages and calculating the cantilever resistance. Since the power (P_2) corresponding to 550 degrees (T_2) is known and zero power (P_1) corresponds to room temperature (T_1), we can find a simply by $a = (T_2-T_1)/(P_2-P_1)$, See Figure C.1.

Knowing the temperature of the tip is extremely valuable information, but to calculate many (WHAT) thermophysical properties of a sample the temperature just below the tip-sample interface must also be know. This is done in step 2 of the calibration process.

Step 2. To obtain the temperature at the surface below the tip, one can follow the work done by Hinz et al.[30] In this work PMMA is globally heated to a uniform temperature and force-distance curves (FDCs) are recorded. Hinz et al. were looking for penetration depth as a function of force applied to the surface with the sample near its glass transition temperature. The

indentation slope of the FDCs decrease and the loading and unloading parts of the FDC separate with increasing temperature compared to a calibration force curve on a hard substrate (Si), which confirms the softening of the PMMA film. FD Curves where conducted on a silicon substrate with the tip at room temperature to measure tip deflection at varying temperatures. Next, using PS (Mw= 215K, 5% b/w in Cyclohexanone and Tetrahydrofuran) and PMMA(Mw= 120K 2.5% b/w in chloroform), FDCs were taken with the tip at room temperature (0 volts on voltage generator) and increasing temperatures until the change in slope and the loading and unloading parts of the FDC started to separate[30] as noted by Hinz. These polymers were chosen due to their well documented glass transition temperatures. Prior to measurements, polymers were spin coated on steel discs purchased from Ted Pella, USA (product Number 16219, 20mm Specimen Disks) and measured the resulting film thickness to make sure the films were thicker than 50 nm, so that to avoid issues of glass transition temperature dependence on the film thickness.[47-48] From the comparison of the obtained glass transition temperatures for PS and PMMA with their literature values,[106] one obtains a calibration relation (see Figure C.1) between the temperature on the surface and the temperature on the tip.

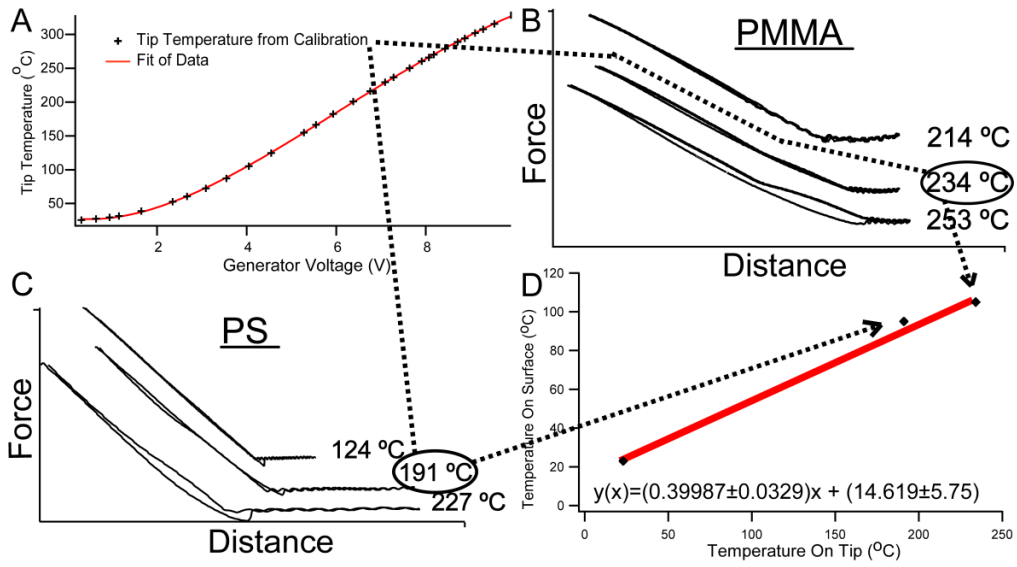

Figure C.1. Calibration details of thermal levers. A) Tip temperature as a function of Generator Voltage (Vs from Step 1) for various Vs (Black crosses) and a polynomial fitted curve. B) Force-Distance Curves on PMMA for tip temperatures below (214°C), at (234°C) and above (253°C) the Tg of PMMA. C) Force-Distance Curves on PS for tip temperatures below (124°C), at (191°C) and above (227°C) the Tg of PMMA, the separation of extension on retraction curves indicates that Ts has reached Tg. D) Linear fit of the calculated tip temperature and the accepted Tg for PMMA and PS with room temperature as reference.

Appendix D. Polymer sample preparation steps

Below are steps used to create the Polystyrene sample used in this thesis. The steps are written as instructions in order to provide anyone wanting to continue this work a guide to reproduce the samples used.

1. Choose a solvent appropriate for the polymer you want to deposit, here PS(American Polymer Standards Corporation, Product #PS215K), M_w=215K and toluene(Sigma-Aldrich, Product #179418) many solvents can be found at the polymer manufactures websites or polymer handbooks.[98, 106]
2. Find the percent solution by weight you need for the thickness of film you want at the end. Here 2.5% solution of PS in toluene was used.
3. Get the density of the solvent (here toluene: 866.5 mg/mL) found on the bottle or the manufactures website, the mg of polymer per 1 mL of final solution is found by:

$$2.5\% \times 866.5 \frac{\text{mg}}{\text{mL}} = 21.6 \frac{\text{mg}}{\text{mL}}$$

4. For example if you want 2 mL of 2.5% by weight solution, you'll need 43.2 mg of PS. Here only one mL of solution was needed.
5. Put on gloves, they are needed for the next steps.
6. Clean a spatula (Ted Pella, product # 13523) by washing it in the following order acetone*, ethanol$^{\Theta}$, isopropanol*(*Fisher Scientific, $^{\Theta}$Decon Labs), DI water, finally dry with nitrogen. Set aside with the scoop end propped up.
7. Zero the scale (here; Scientech ZSA 210), weigh an eppendorf (Eppendorf North America, product 022363204) and re-zero the scale.
8. With the spatula add polymer into the eppendorf until you reach the amount needed (here: 21.6 mg).
9. With a pipette, get the amount of solvent you need, here 1 mL, and pour the solvent in the eppendorf with the polymer.
10. Close the cap of the eppendorf and place on the vortex mixer (Southwest Science, BV1000) until you cannot visually see any polymer.
11. Retrieve a new eppendorf, a 0.45 μm filter (TPP model#99745) and a syringe (Becton Dickinson & Co, Model 309623) with a needle.
12. Carefully draw the solution into the syringe through a needle attached, remove the needle, then attach the 0.45 μm filter to the syringe.
13. Open the new eppendorf, line up the filter exit with the eppendorf, and slowly but firmly push the plunger until the solution is in the new eppendorf. Close the cap when finished and label the eppendorf appropriately. Set aside.
14. Choose the substrate, here silicon (Silicon Materials Inc. Part# 3NO 5-10 381-20-5) was chosen.

a. When cutting the Si with the diamond cutter:
    i. Wear gloves, eye protection
    ii. The shape of the final piece of Si should be symmetric, squares are easiest.
    iii. Score a straight line on the Si wafer, Figure D.11-3. The unmounted Chip Carrier Toolkit (Bruker USA, Product# APCC-0001) is marked to help scoring a line and to break the Si wafer as cleanly as possible.
    iv. To beak the Si, align with the steps on the tool kit and gently press down.
    v. Rotate and repeat scoring, then break Figure D.1 4-6.

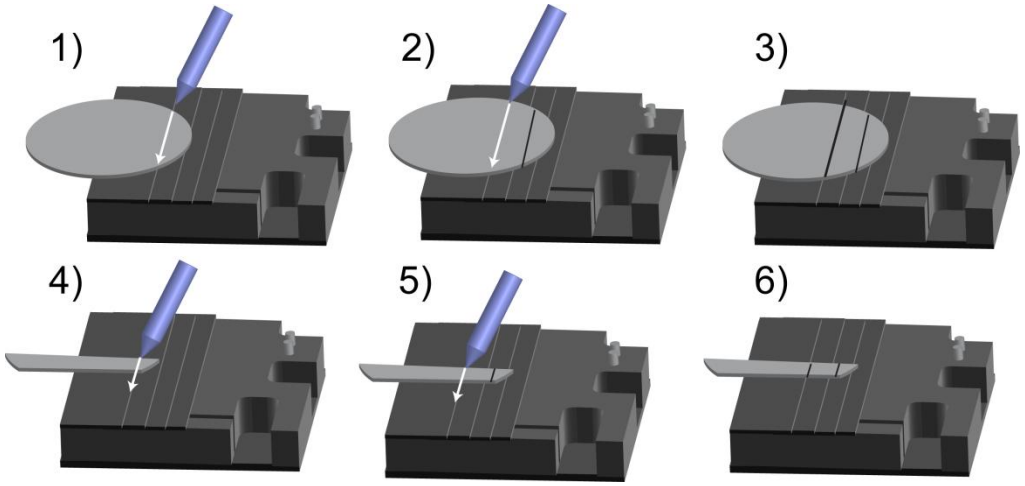

Figure D.1. Steps for cutting substrate for sample preparation.

15. Clean a pair of AFM tweezers (Ted Pella, Product #5599), in this order: acetone, ethanol, isopropanol, DI water, finally dry with nitrogen. Set aside with the "pick up" end propped up.

    In the following steps it is implied that Si is manipulated with the clean tweezers.

16. Get four 10 mL glass beakers, fill individual beakers with a few mLs of acetone, ethanol, isopropanol, and DI water. Don't mix solvents, you'll have one beaker with acetone one with ethanol, and so on.
17. Rinse the SI square with DI water from the squirt bottle to remove any chunks from cutting, dry with nitrogen.
18. Place the Si in the beaker containing acetone, cover the beaker with parafilm.
19. Follow the manufacturer's instructions for the sonicator (Branson Ultrasonics Corporation, Model 2510) and sonicate the beaker for 10 minutes, remove and dry with nitrogen.
20. Repeat step 19 for ethanol, isopropanol, and DI water. Be sure to do steps 21 & 22 before the end of the final sonication.

21. Rinse an AFM sample disk (Ted Pella, Product# 16219, 20mm) with acetone, (ethanol, isopropanol,) and DI water, dry with nitrogen. Place on a clean piece of lens paper.
22. Place an adhesive tab (Ted Pella Product #16082) in the center (best you can) of the AFM sample disk, press firmly with a gloved finger to remove any air trapped between the disk and tab.
23. Take the clean SI square and gently place centered on the adhesive tab.
24. Open the tweezers to the diagonal width of the Si square and gently press the four corners, two at a time into the adhesive tab. If needed you can press parts of the squares parameter into the tab also to remove the air between the Si and the tab. Do not touch the central portion of the Si square with the tweezers. See Figure D.2.

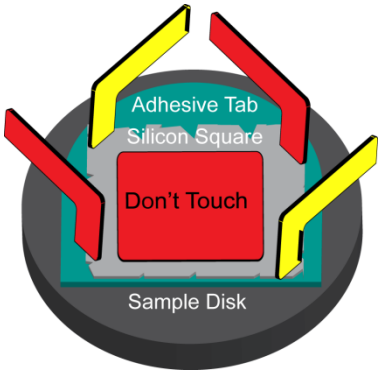

Figure D.2. Locations to adhere substrate. Locations to press the Si square to avoid damaging central area and minimize air bubbles. The different color tweezers ends indicate that opposite corners are secured simultaneously.

25. Place the disk with Si square in a clean petri-dish and cover.
26. Take a 10 µL pipette and an appropriate size tip; fill a 10mL beaker with Di water, practice getting a drop of water to form and fall from the tip. This µL setting is approximate due to the properties of the water verses the solution but will give a rough estimate for the solution. Once finished discard the tip.
27. Follow the instructions posted to set up the spin coater (Laurell Technologies Corp Model WS-400E-6NPP-LITE) and spin program, here the program was 10 seconds at 500 RPM and 50 second at 2000 RPM.
28. Once the program is set and the disk is secured by the vacuum on the chuck, run the program to make sure it is correct.
29. Place a new tip on the 10 µL pipette and open the eppendorf from step 13 (the one with the 2.5% solution), practice a few times with the pipette letting to drop fall back into the eppendorf. Record the setting on the pipette that gave a satisfactory drop.
30. Draw solution into the pipette tip and place a drop on the center of the Si square, don't touch the Si with the pipette tip, repeat until a bead of solution is on the Si that you know will cover the Si when spun.
31. Run the program.
32. Remove the sample and place in a clean container.
33. Clean the spin coater according to the posted instructions.
34. If you do not plan to anneal the sample skip to step 41.

35. To anneal: warm up the hot plate (Fisher Scientific, Model Isotemp) at this point, get the thermocouple (Cen-Tech Model p37772) and prop the senor end so that is rests on the plate, do not trust the reading on the hot plate itself (inaccurate).
36. Find the glass transition temperature for the molecular weight (bulk) of the polymer you're using. Glass transition is a function of the film thickness and normally decreases when the film is less than 150 μm thick, so if you are attempting a thinner film, a scratch test or other method of determining film thickness may be needed. The final temperature on the plate used here was 85°C by the thermocouple, 95° C was the value for bulk but the expected film thickness was greater than 200 μm.
37. Anneal the sample, here 14 hours, remove and allow cooling to room temperature.
38. Use the AFM to image the sample. You're checking for pits and overall quality, here after 14 hours, 20 μm x 20 μm scans reveled many 2-4 nm deep pits. The polymer sits above the hot plate and has the Si, adhesive tab and disk between it so most likely the polymer was not at 85°C.
39. You can anneal above glass transition to further remove unwanted surface features, this sample was annealed a second time at 120°C for 2.5 hours. Caution is advised though. These instructions haven't mentioned to this point that three samples of PS at different molecular weights were being made. Why? Because two were destroyed at this point.
40. Following the second annealing, the sample was allowed to cool, and a scratch test performed to determine film thickness.
41. Scratch test:
    a. Heavily rinse a new razor blade with acetone, ethanol, isopropanol, and DI water in that order and dry with nitrogen.
    b. Angle the blade so that one end will cut the polymer and gently pass the blade over the sample through the center.
    c. Observe the scratch under the optical microscope; if the blade successfully cut through the thickness of the polymer you see the Si substrate in the scratch.
    d. Image scratch with AFM. Note: In most cases the tip will encounter a sharp topography change of 100-300 nm while imaging the scratch. For an accurate measurement cantilever selection and feedback settings are crucial.
42. Finally ensure that sample preparation notes and all AFM measurements are documented for later use.